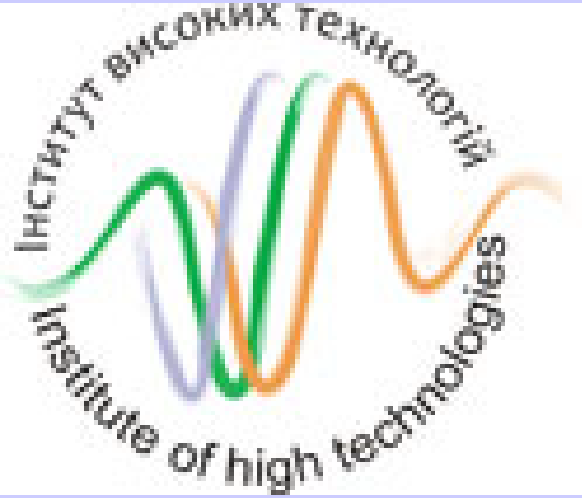

Застосування наноматеріалів для хімічних сенсорів та в діагностиці

проф. В.А.Скришевський

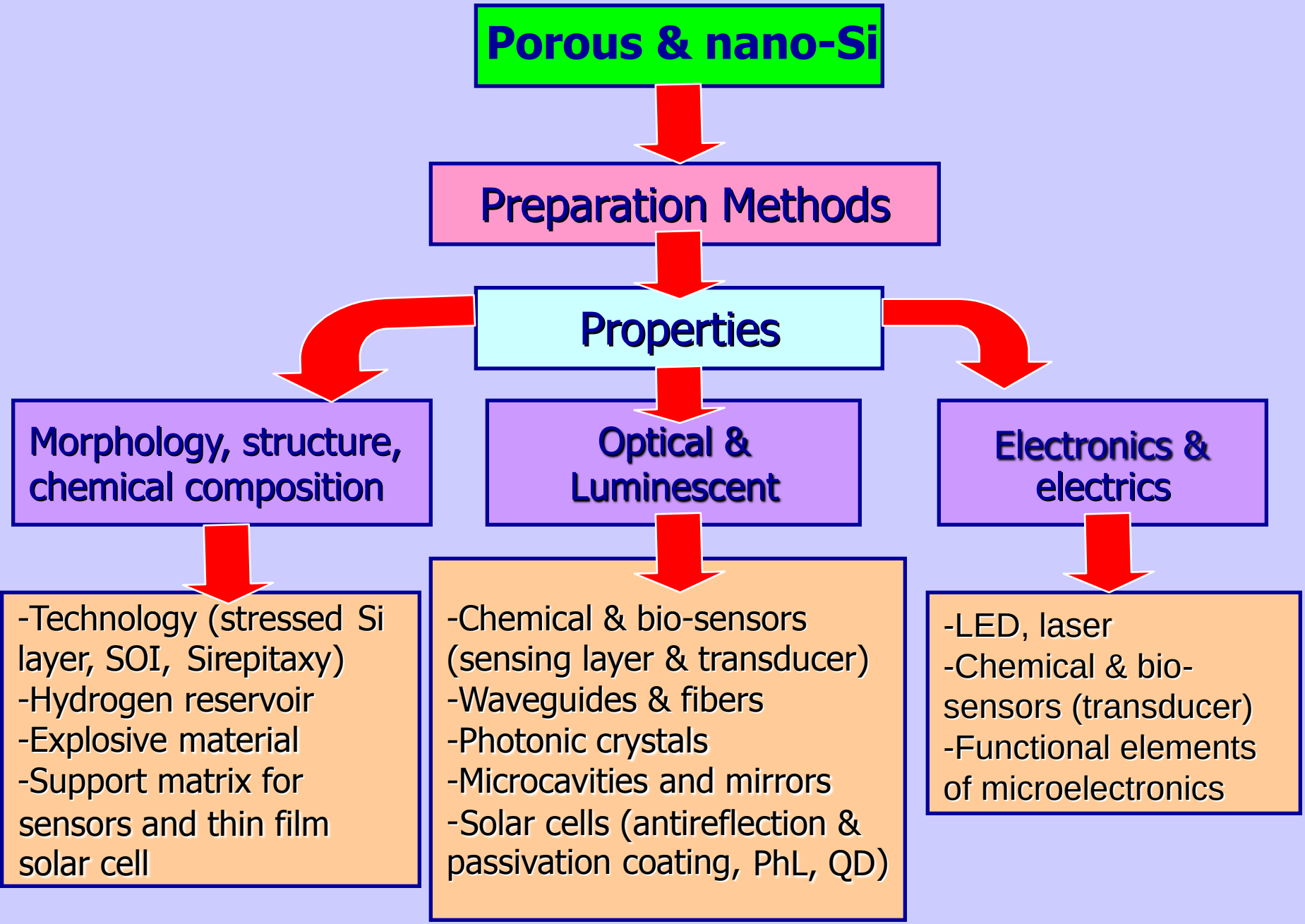
Porous & nano-Si
Preparation Methods
Properties
Morphology, structure, chemical composition
Optical & Luminescent
Electronics & electrics
-Technology (stressed Si layer, SOI, Sirepitaxy)
-Hydrogen reservoir
-Explosive material
-Support matrix for sensors and thin film solar cell
-Chemical & bio-sensors (sensing layer & transducer)
-Waveguides & fibers
-Photonic crystals
-Microcavities and mirrors
-Solar cells (antireflection & passivation coating, PhL, QD)
-LED, laser
-Chemical & bio-sensors (transducer)
-Functional elements of microelectronics

Electroluminescence of porous Si (injection-type in Schottky contact)

Requerements:

λ=0.4-0.7 μm (displays), 1.3-1.6 (optical fibers)

Emitting power in mW range

Operating voltage <5 V

Modulation frequency- few kHz (display),

> Few GHz(communications)

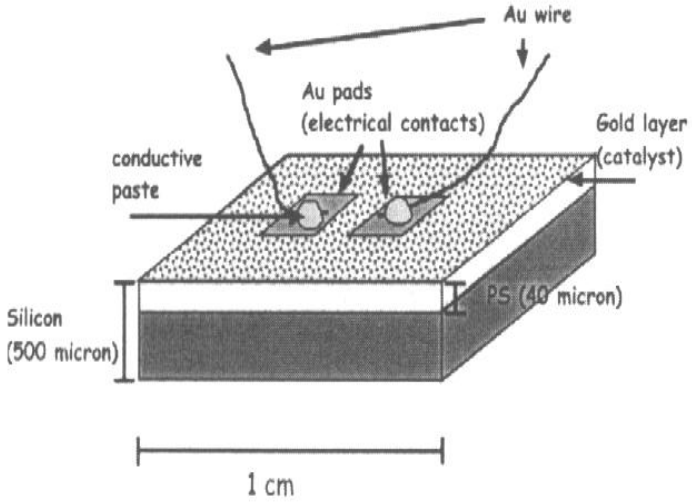

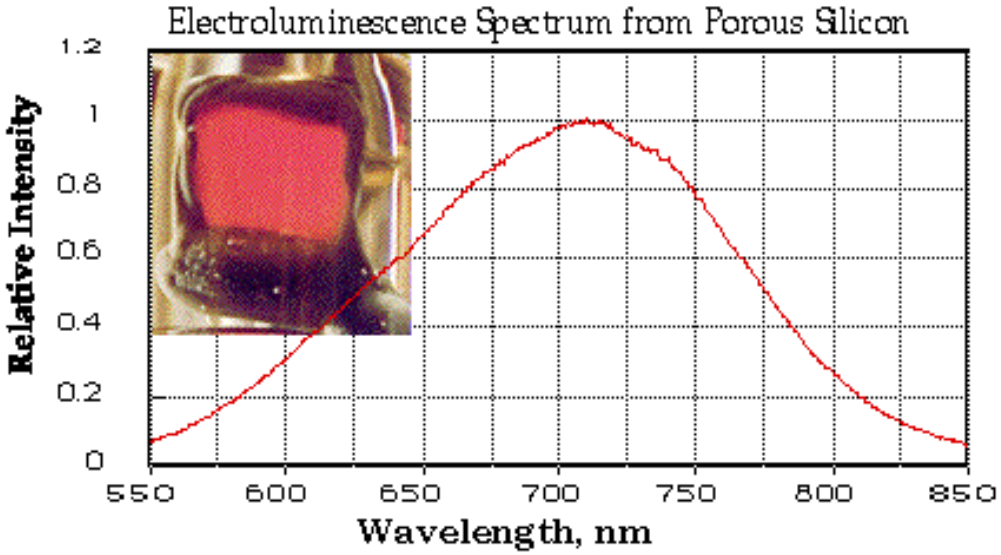

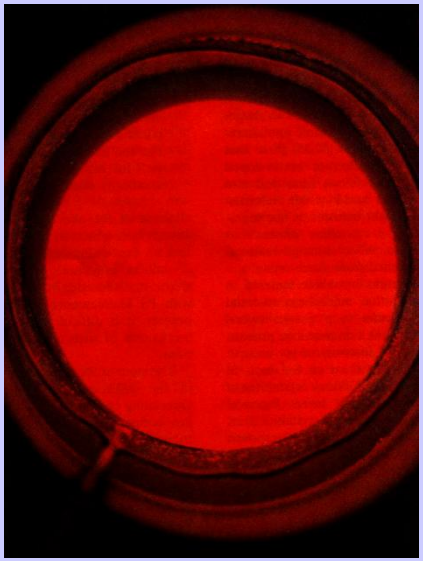

Bomchil et al., Appl. Surf. Sci., 65/66, 1993

Problems:

η_{EL} < 1% in solid!

η_{PhL}>10%

Photoluminescence sensors
Quenching effect

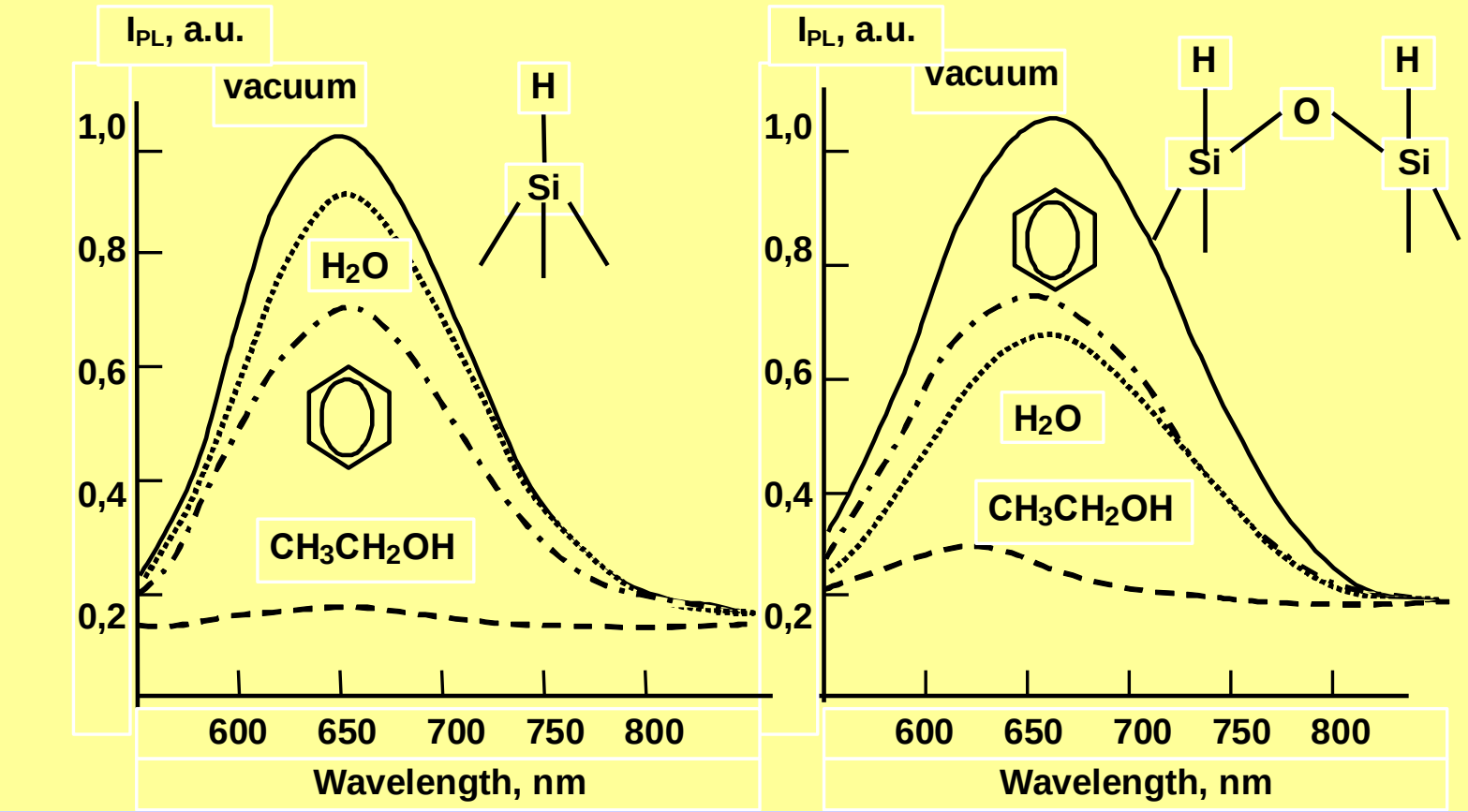

Hydrophobic surface

Hydrophilic surface

PL spectra of as-prepared (a) and oxidized (b) PS in vacuum, H_2O, benzene, ethanol

*I*J.M.Lauerhaas, M.Sailor, Science, 261, 1567,1993)/

Photoluminescence quenching

Reversible quenching (physisorbed): alcohols (ethanol, methanol), aromatic (pyrene, anthracenes, benzene, toluene), acid, base….

Irreversible quenching (NO, NO_2, Cl_2, Br_2, I_2, O_2..)
(due to introducing surface non-radiative carrier traps)

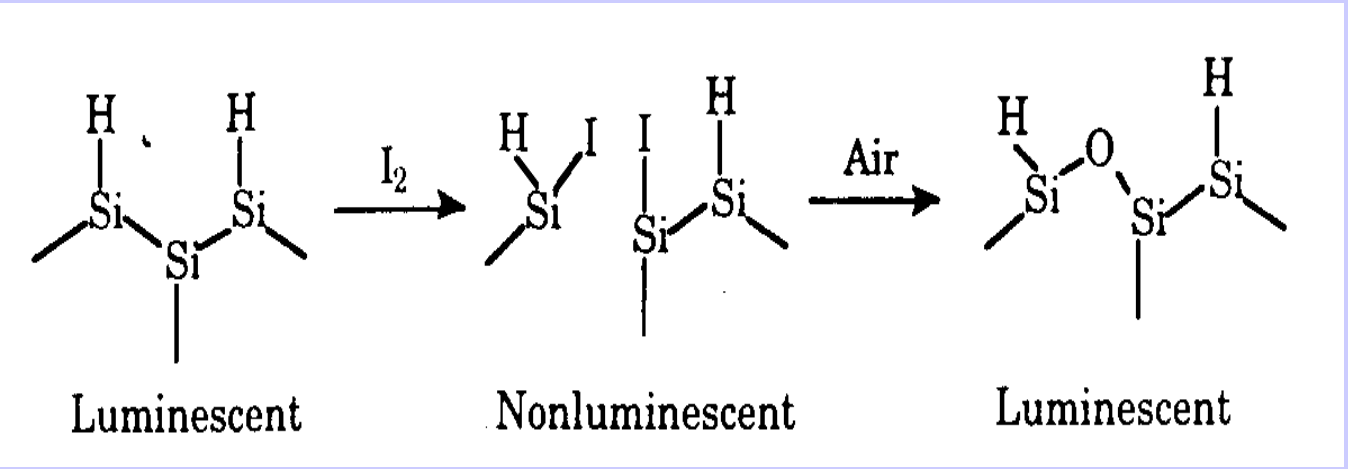

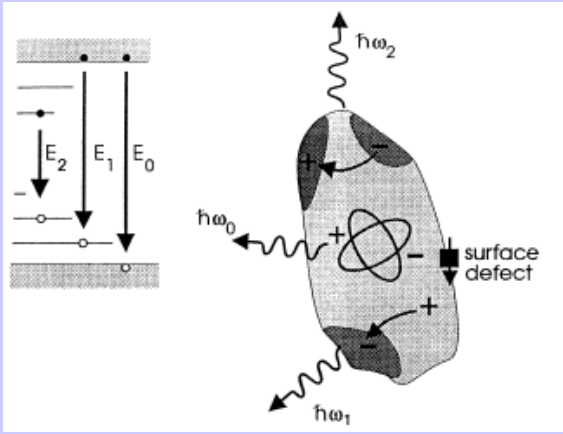

$$\eta_{PL} = \frac{P_{re}}{P_{re} + P_{nre}}$$

Mechanisms of quenching:

- the increase of the non-radiative recombination rate in the nanoparticles due to the alteration of ε
- the change of the nanoparticle electronic structure
- the capture increase on the non-radiative traps at the forming of the strain-induced defects when molecules are adsorbed.

Impact of molecule adsorption on PhL

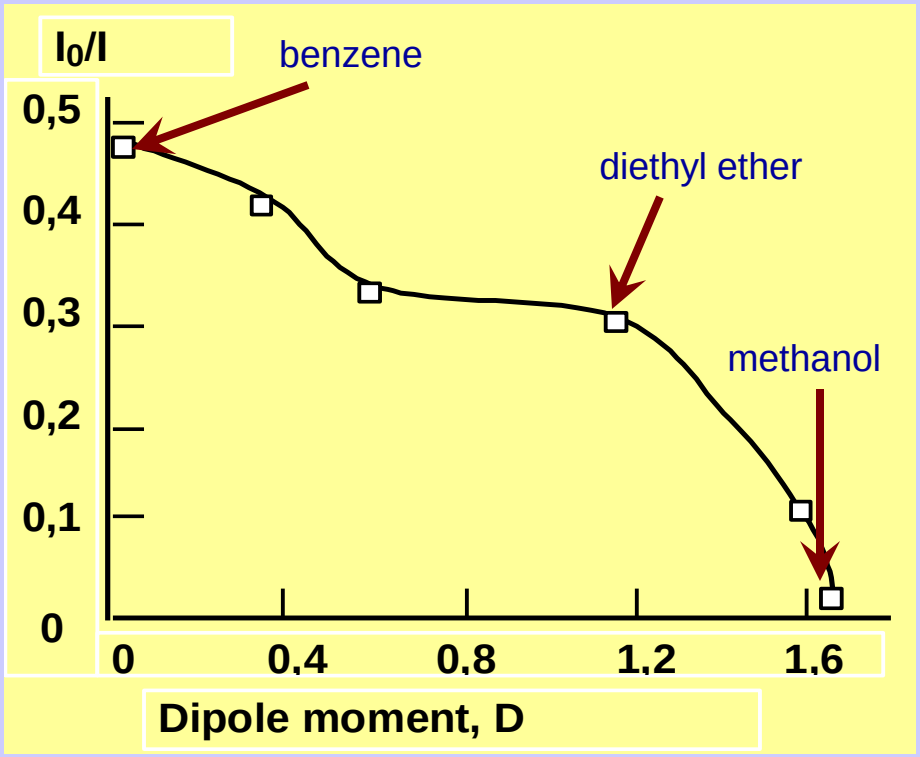

$$p = er$$

PhL intensity versus dipole moment of adsorbates

*I*J.M.Lauerhaas, M.Sailor, Science, 261, 1567,1993)/

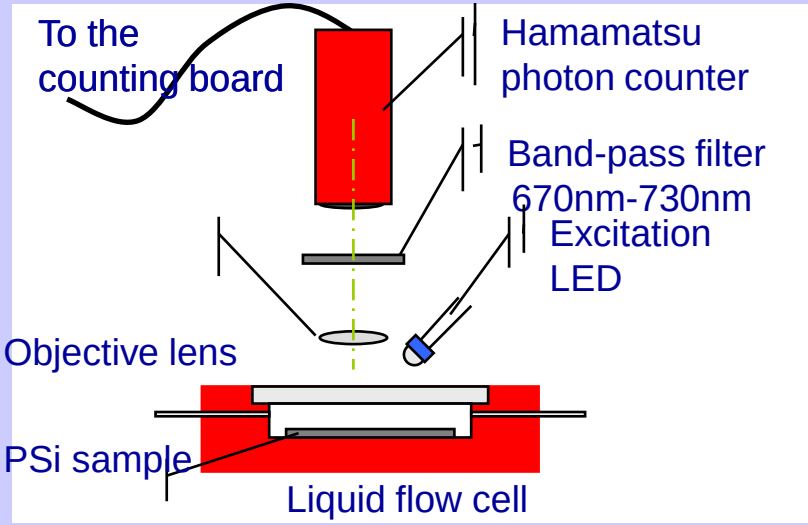

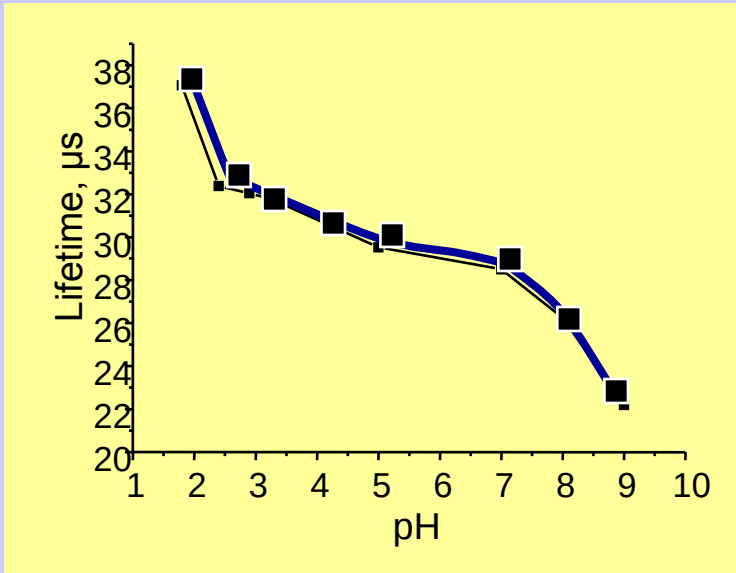

PL decays time versus solution pH

A. Benilov, V. Skryshevsky, Sensors&Actuators, 2007

Optical sensors. Wave guiding

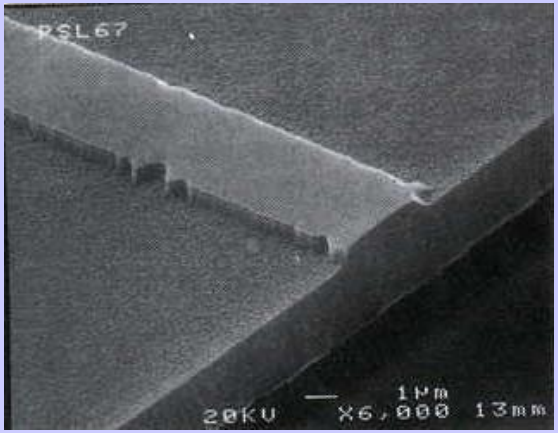

Multilayer Planar Waveguide

G.Loni,Thin Solid Film 276(1996)143

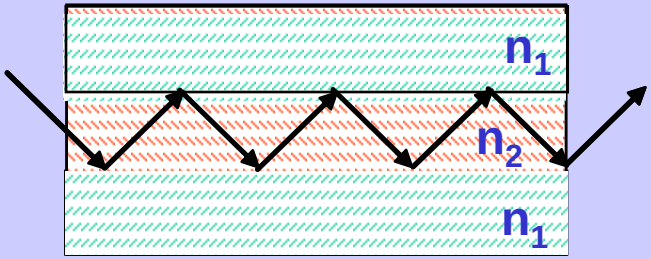

internal reflectance

$n_2 > n_1$

$$\theta_c = \arcsin\left(\frac{n_2}{n_1}\right)$$

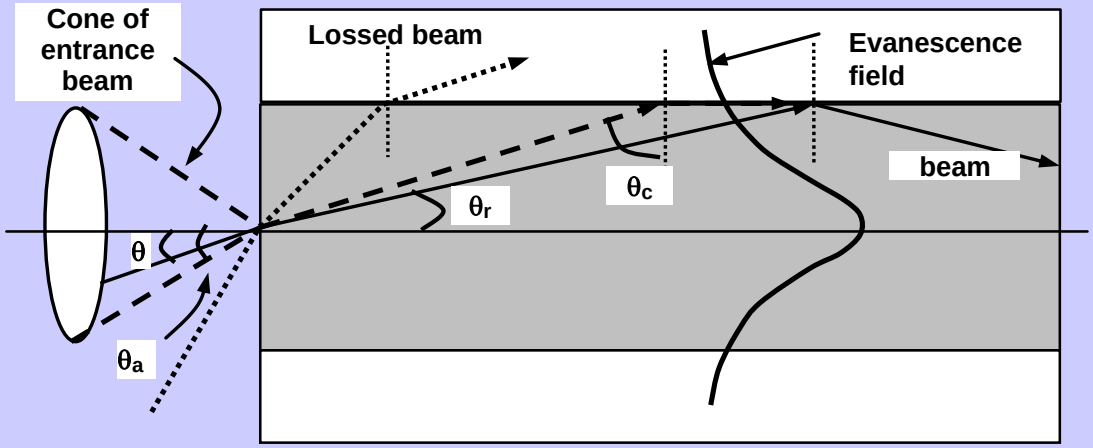

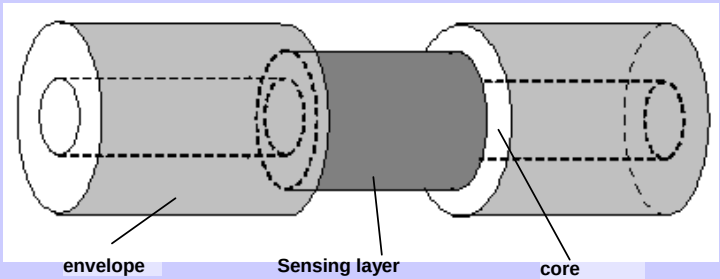

$$d_p = \frac{\lambda}{2\pi\sqrt{(n_1^2 \sin^2\theta_1 - n_2^2)}}$$

Types of optical sensors

Bragg-reflector

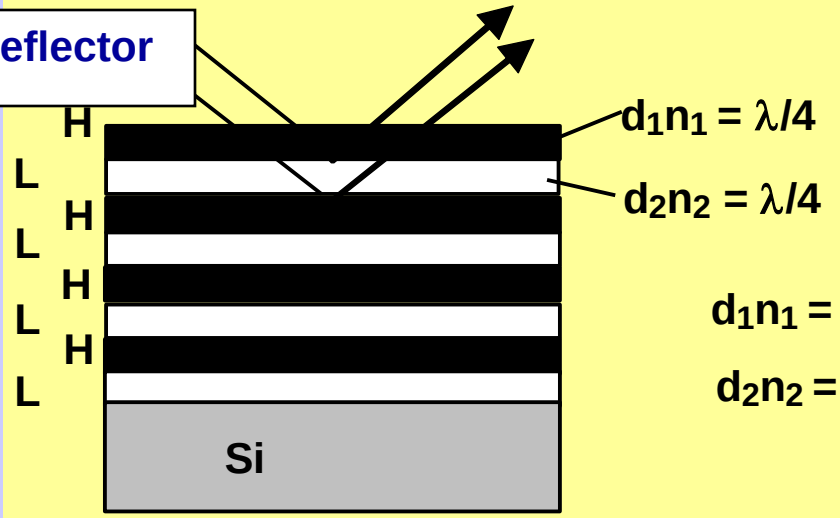

Fabry-Perot- filter

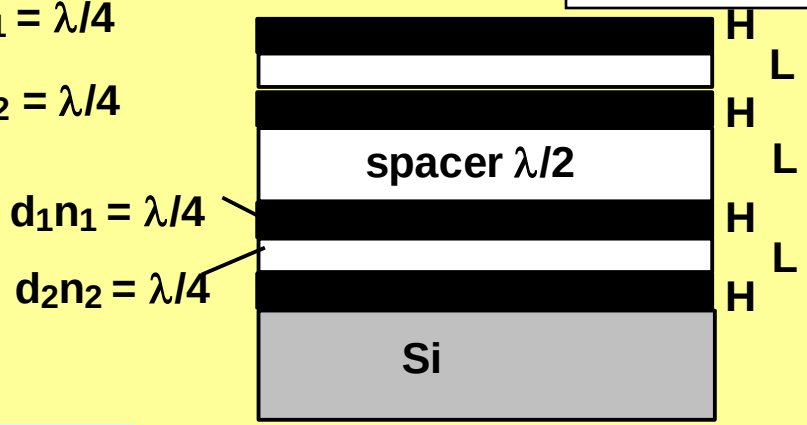

$$n_A d_A + n_B d_B = \lambda/2$$

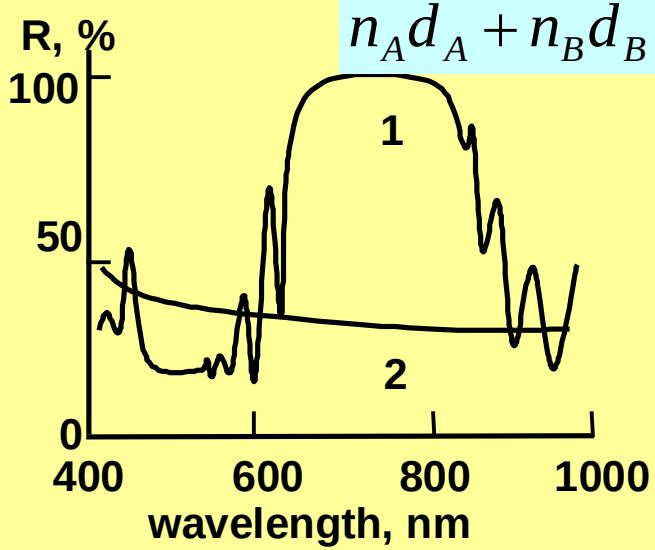

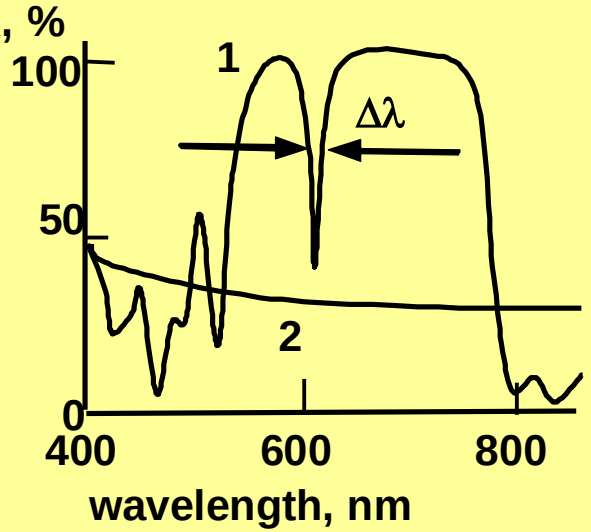

/M.Thonissen, In: "Properties of porous silicon", ed.L.Canham, Emis, N18, 1997, p.349/

Adsorption in porous silicon

Dipole adsorption – the change of charges on surface states

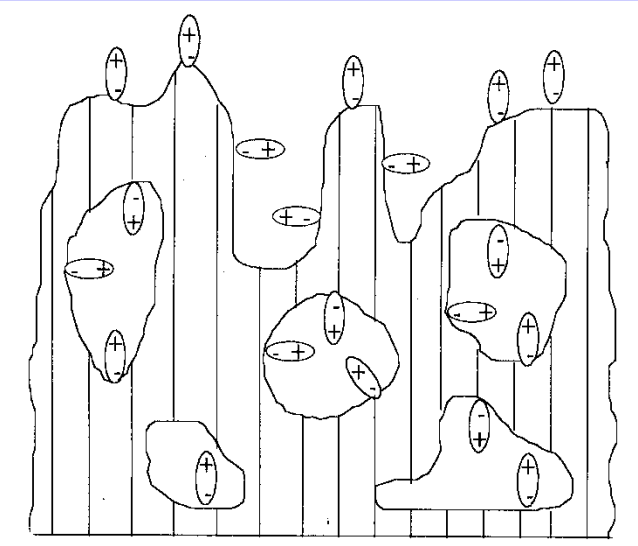

Adsorption in PS: on surface and developed bulk

Adsorption of noncharged particules

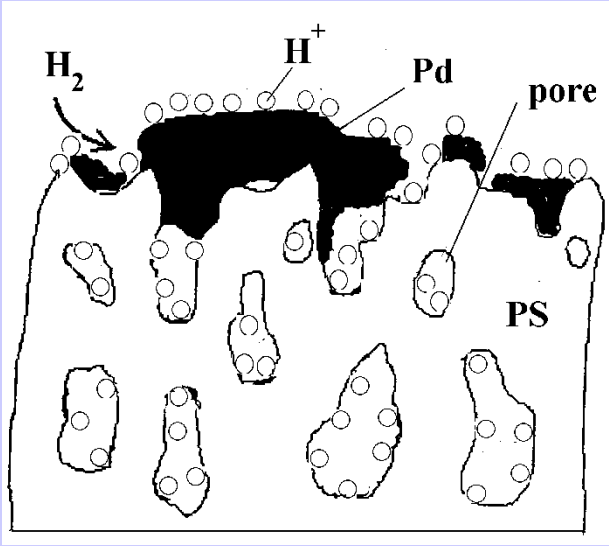

Porosity: $P=U_p/(U_s+U_p)$, where U_p , U_s – volume of pore and Si

Permittivity of PS : $\varepsilon_{PS} = (1-P)\varepsilon_s+P\varepsilon_p$

After adsorption: $\varepsilon_{PSa}=\varepsilon_{PS} +6P(d_a/d)(\varepsilon_a-\varepsilon_p)$

EXAMPLE: $\varepsilon_{PS} = 5.3$ *for PS (porosity P=0.6, pore diameter d=5 nm)*

$$n_{PS} = \sqrt{\varepsilon_{PS}}$$

After H_2O adsorption ($\varepsilon_a = 80$) ⟹ $\varepsilon_{PSa} = 62$

Optical bio – sensing in microcavity

Recognition and binding of bacteriophage lambda DNA

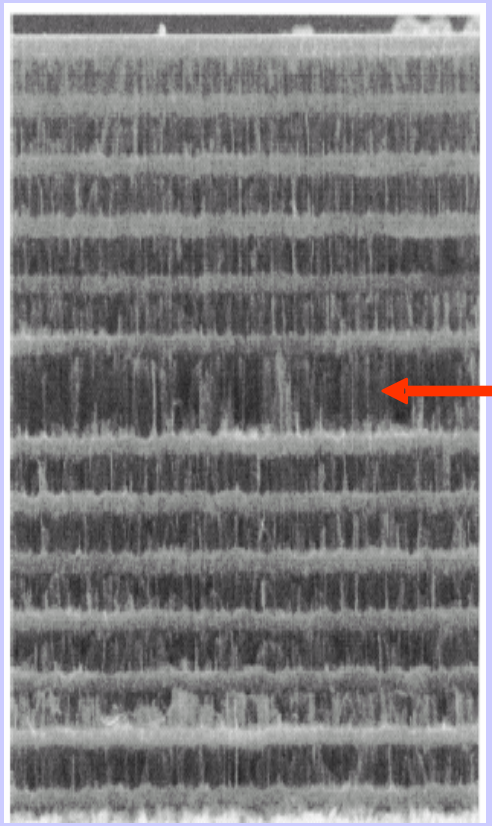

Bragg's mirror

Photoluminescent microcavity

Bragg's mirror

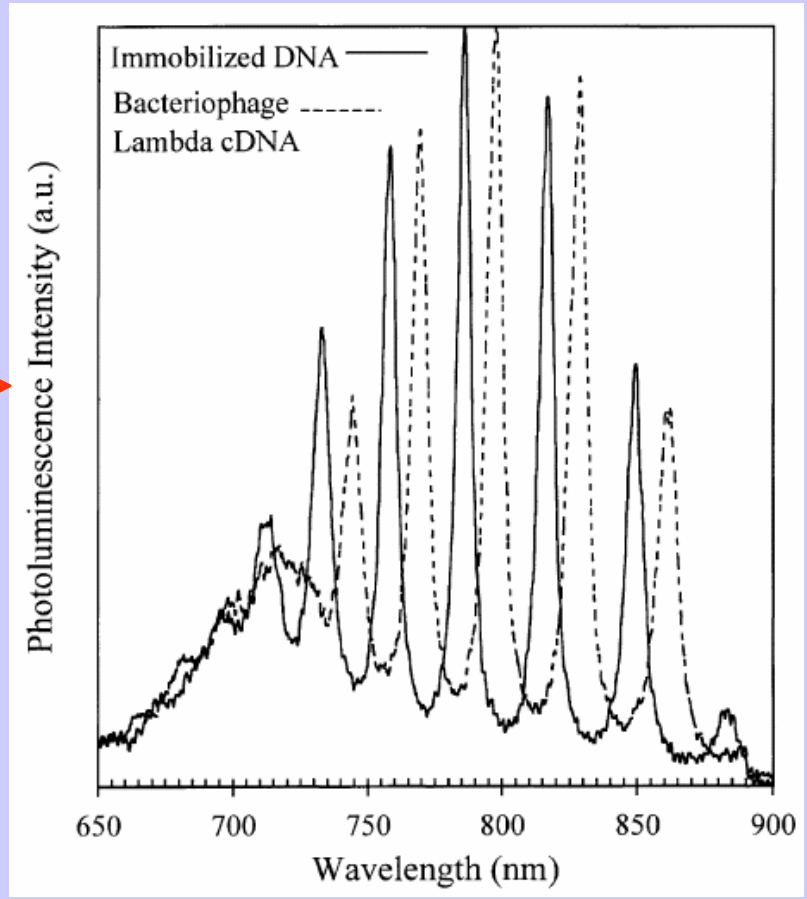

S.Chan et al, Mat.SciEngin,C15(2001)277

Fine tuning of the dichroic behaviour of Bragg reflectors

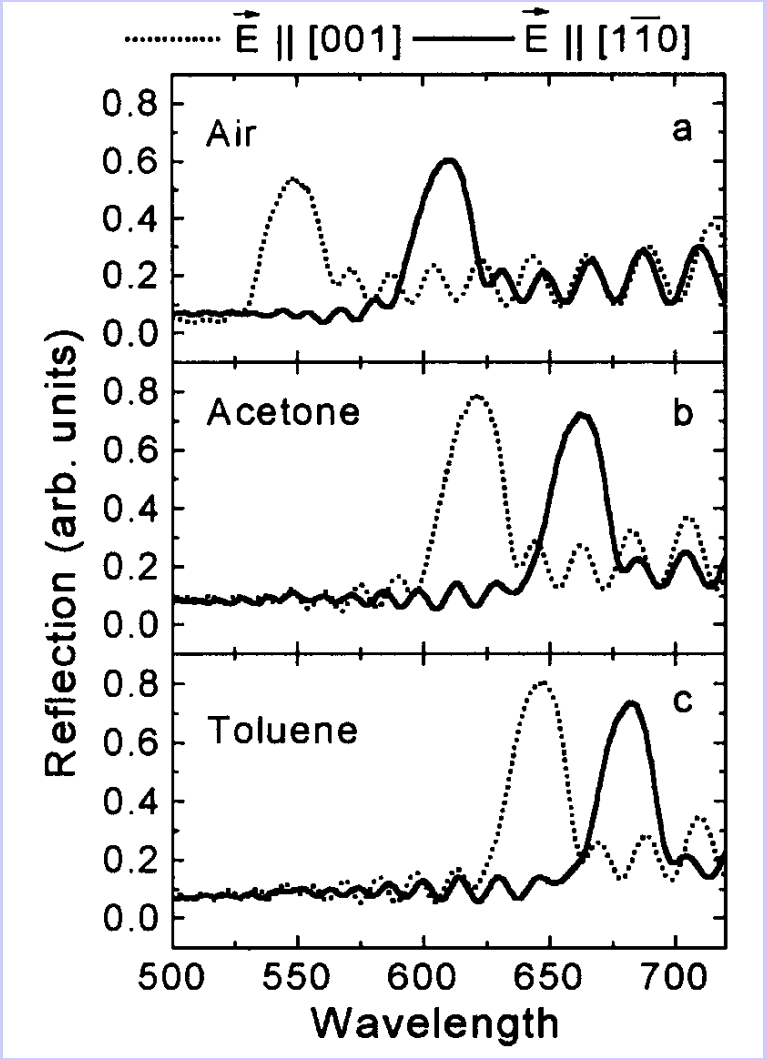

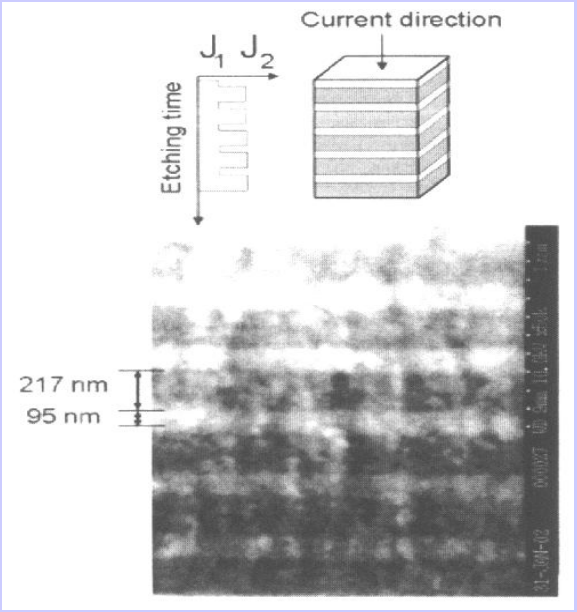

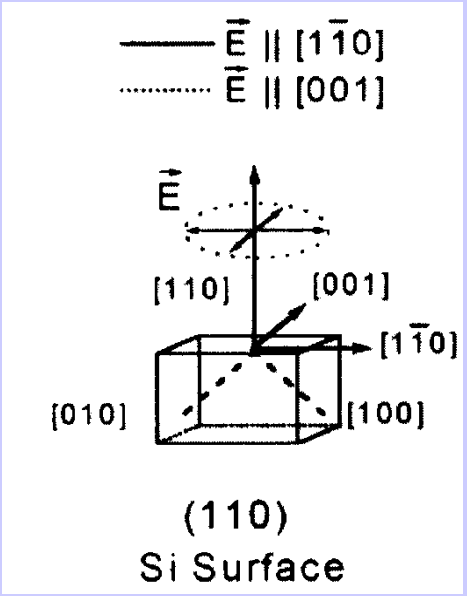

$$n = \frac{1}{2d}\left(\frac{1}{\lambda_r} - \frac{1}{\lambda_{r+1}}\right)^{-1}$$

J.Diener, et al., phys.stat.sol 197 (2003)582

Electrical gas sensing

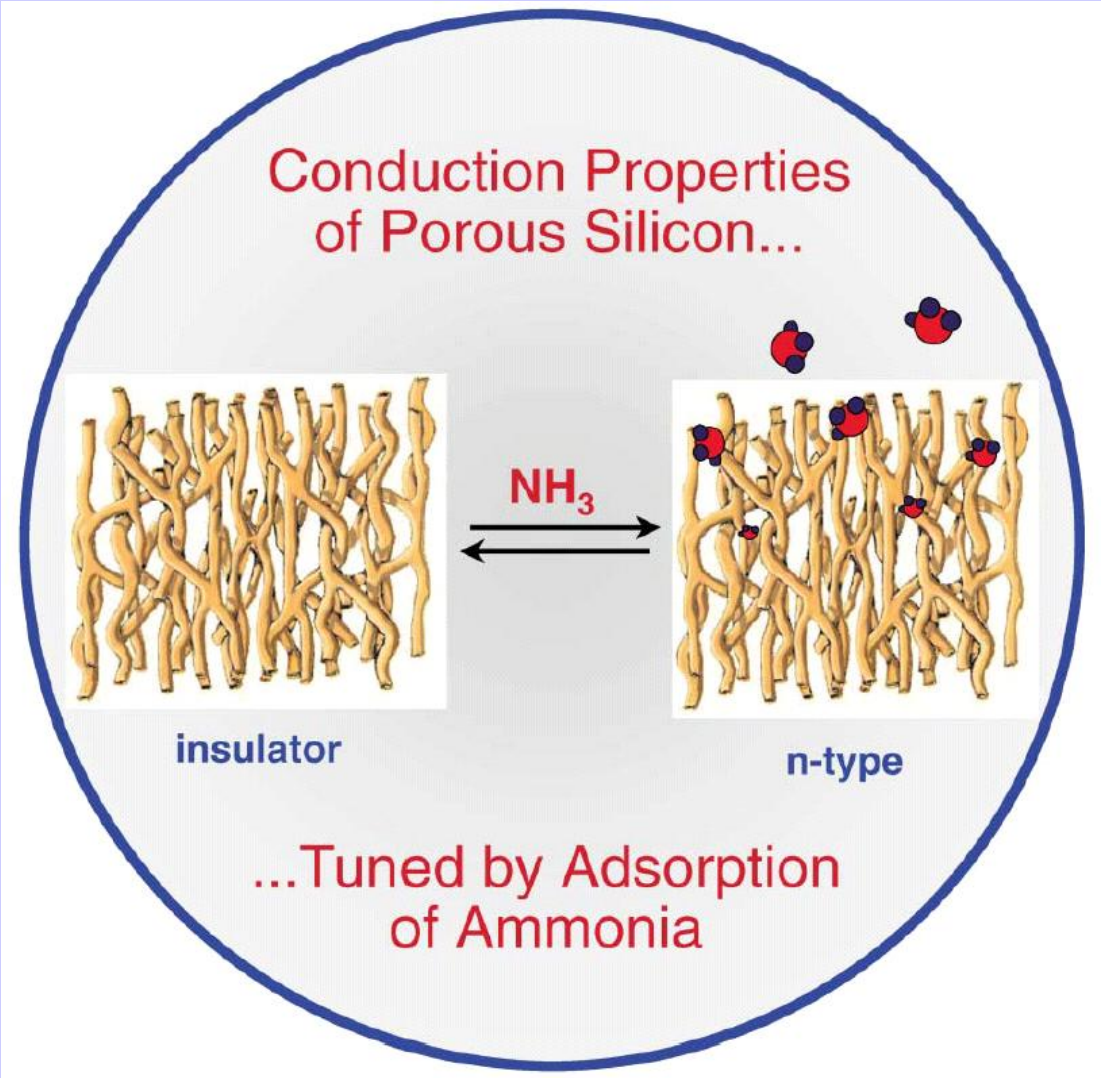

PS Sensor of NO_2

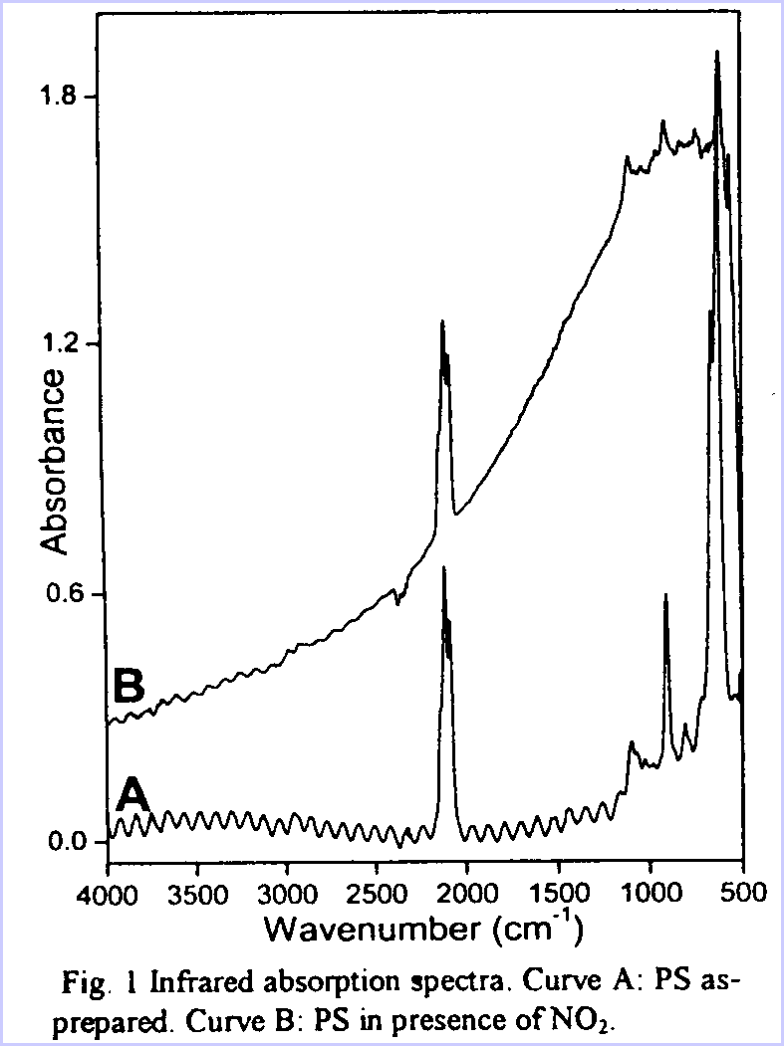

Fig. 1 Infrared absorption spectra. Curve A: PS as-prepared. Curve B: PS in presence of NO_2.

C.J.Oton, et. al., phys.stat.sol, **197** (2003)523

Drude model: $\alpha \sim \lambda^2$

Polarization effect: the induced conductivity at the polar NO molecules adsorption into pores

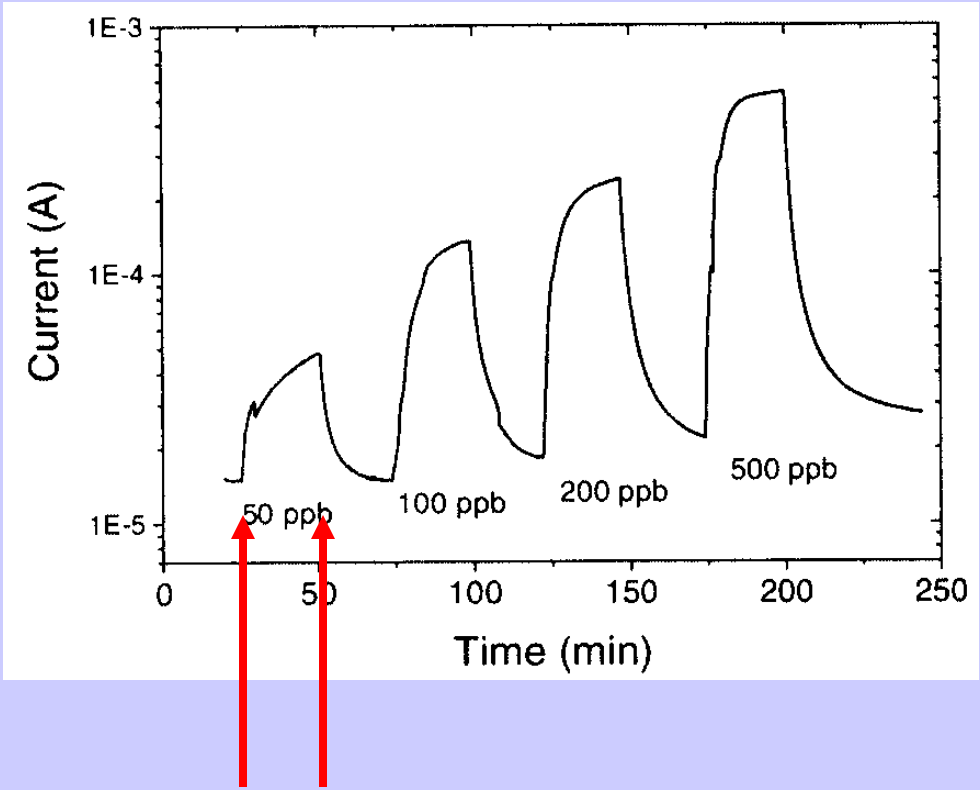

E.Garrone, et al, phys.stat.sol, **197** (2003)103

Interaction of species at semiconductor surfaces

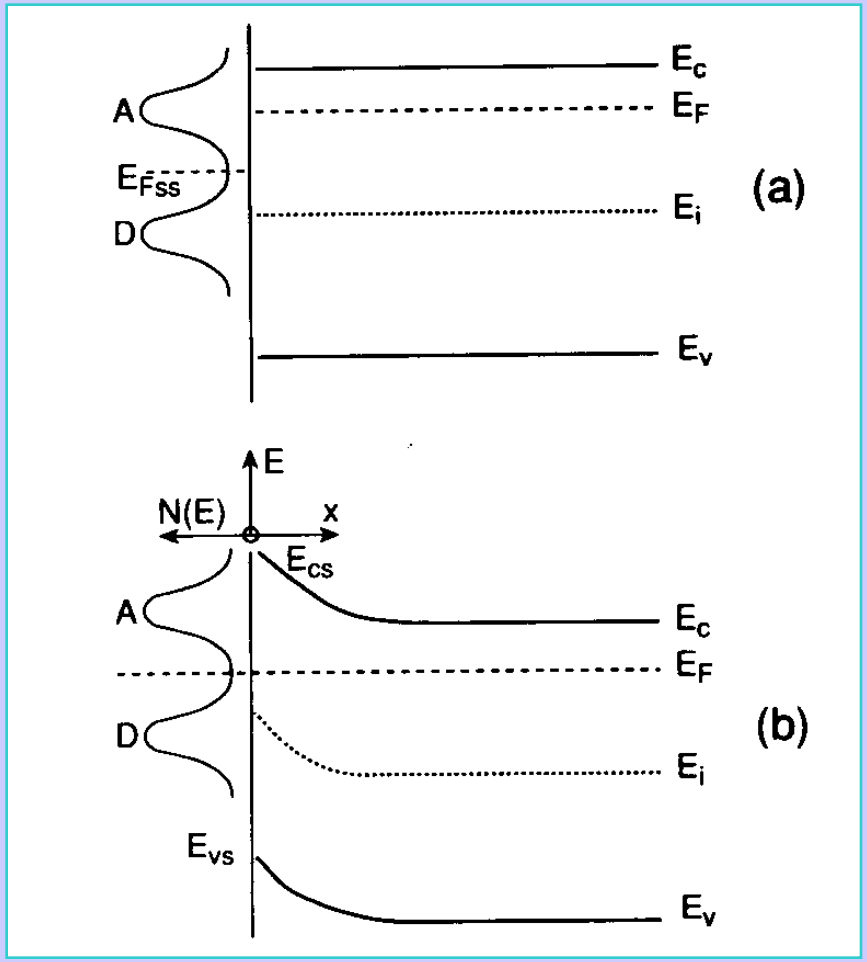

Broken bonds on semiconductor surface form the adsorbing sites for adsorption

Band model of semiconductor surface show the overcharging of surface species:

a- no charge exchange between the semiconductor and surface states;

b- the band bending where e^- from the surface region of semiconductor have moved to surface states to reach equilibrium.

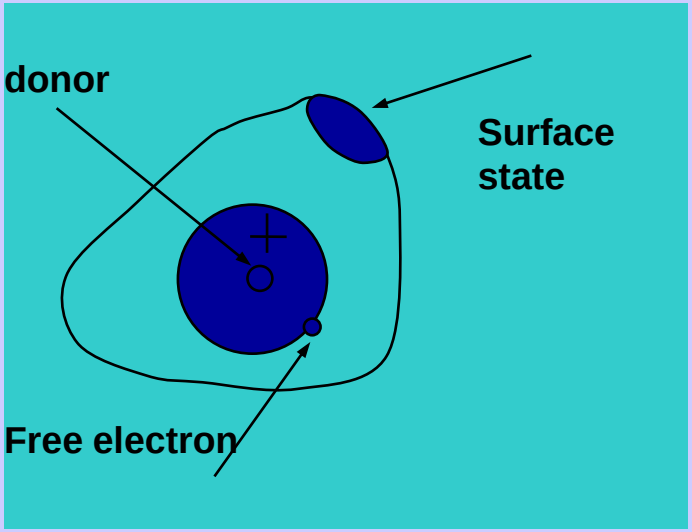

Interaction of gaseous species at semiconductor surfaces

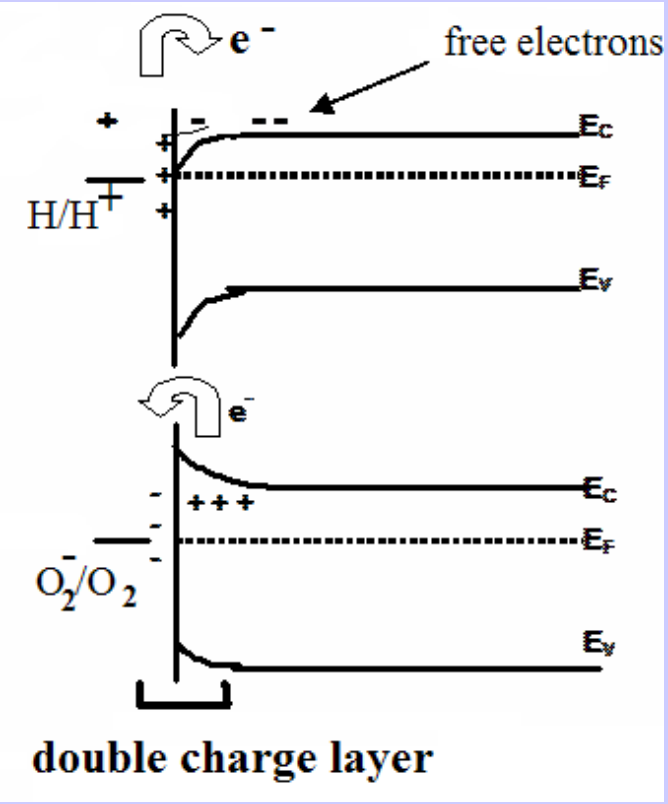

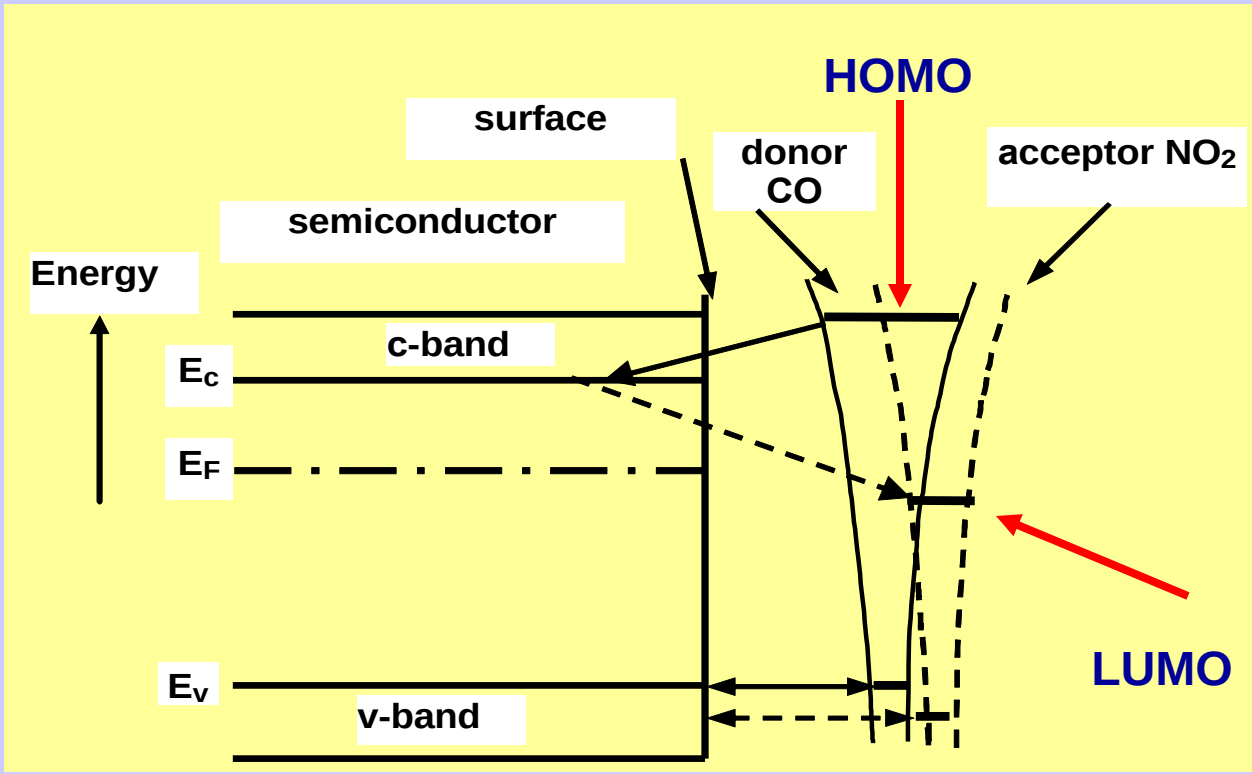

$$C = e\frac{dN}{d\psi} = \frac{\varepsilon\varepsilon_0}{d}$$

The types of adsorbates:
Reducing agents (injection of e^- to bulk):

$$H_2 \rightarrow H^+ + H^+ + 2e^-$$

Oxiding agents (accept of e^- from bulk):

$$O_2 + 2e^- \rightarrow 2O^-$$

Adsorption of molecules in porous materials

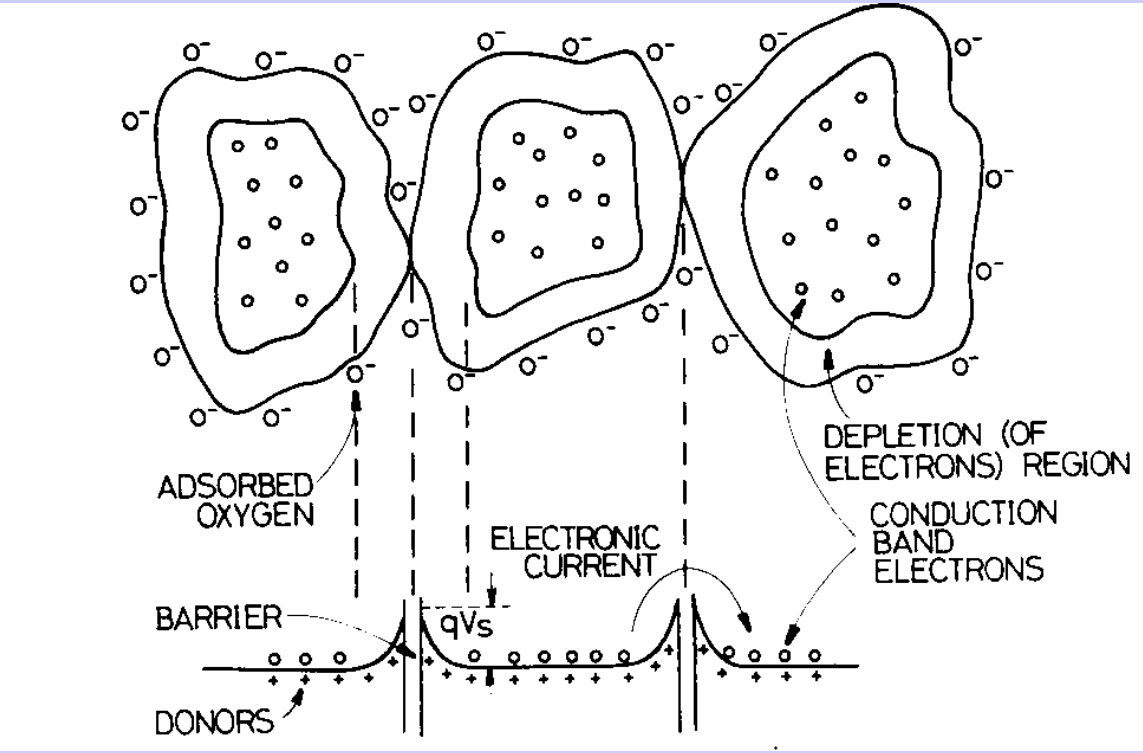

$$\left[O_2^-\right] = N_s = N_D x_0$$

$$e\psi_s = \frac{e^2 N_D}{2\varepsilon\varepsilon_0} x_0^{\,2} = \frac{e^2 N_s^{\,2}}{2\varepsilon\varepsilon_0 N_D}$$

$$n_s = N_D \exp\left(-\frac{e\psi_s}{kT}\right)$$

$$G = \frac{1}{R} = G_0 \exp\left(-\frac{e\psi_s}{kT}\right)$$

Adsorption of proton increases the potential barriers between micrograins, adsorption of oxygen decreases these barriers

Porous Silicon Conductivity

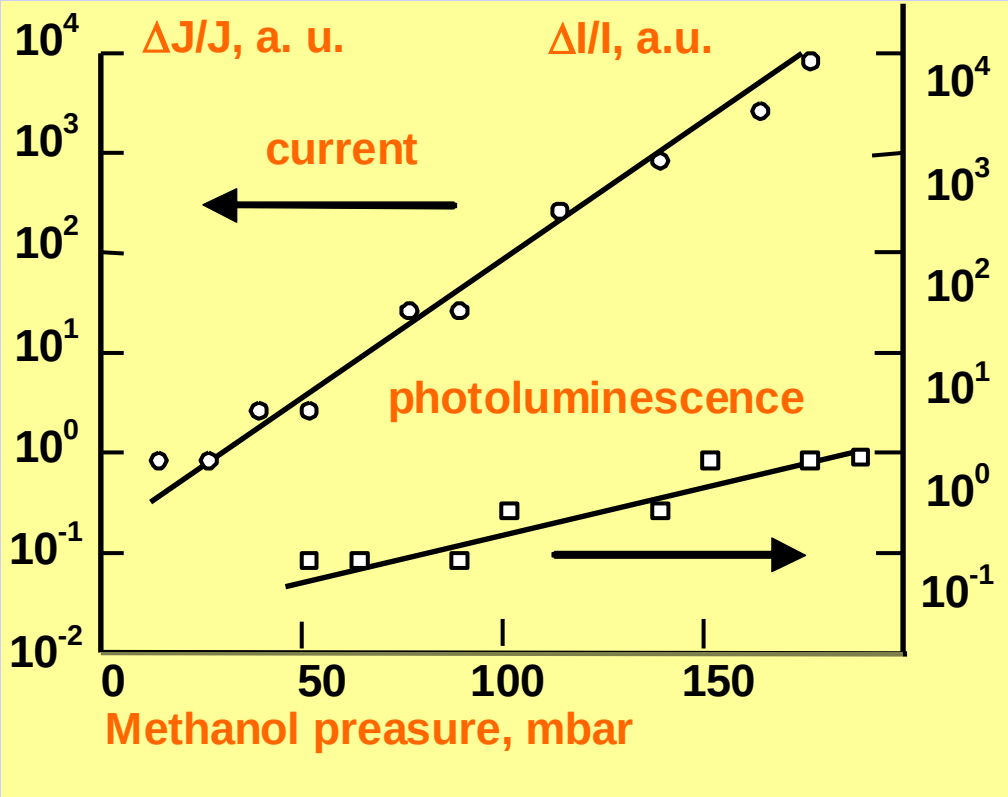

Models for conductivity:

1)the adsorbates make lower the energy barriers between nanoparticles in nanosize Si
2)the change of dielectric constant of nano-Si
3)the charge redistribution inside the nanocrystallites due to the surface states
4)the adsorbates injects extra carriers into nano-Si (reduction-oxidation reactions)

M.Ben-Chorin, A.Kux, I.Schechter, Appl.Phys.Lett, 64, 481 (1994)

2 electrodes transducer

Gold-catalyses PS sensor for NO_x

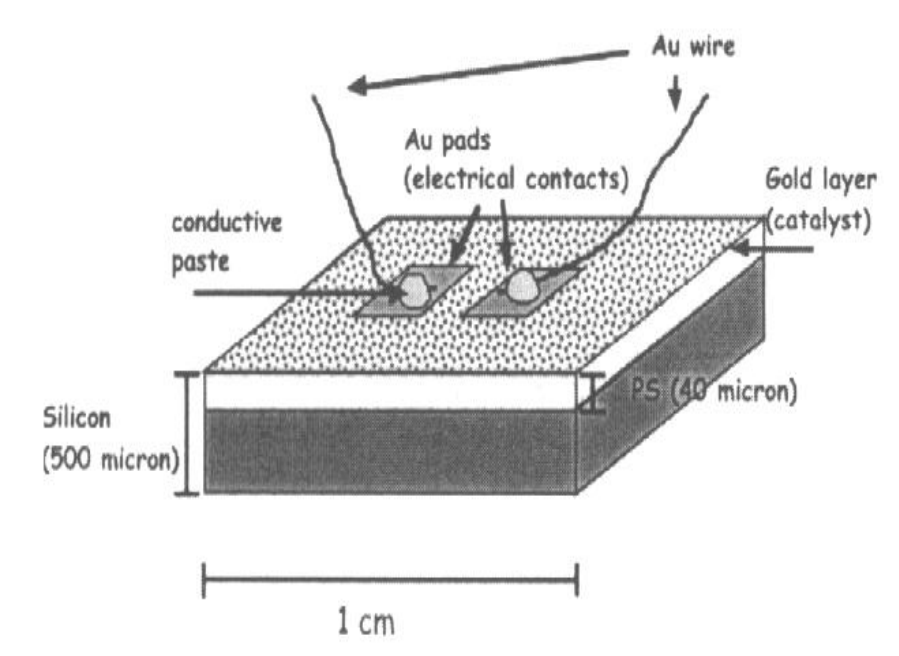

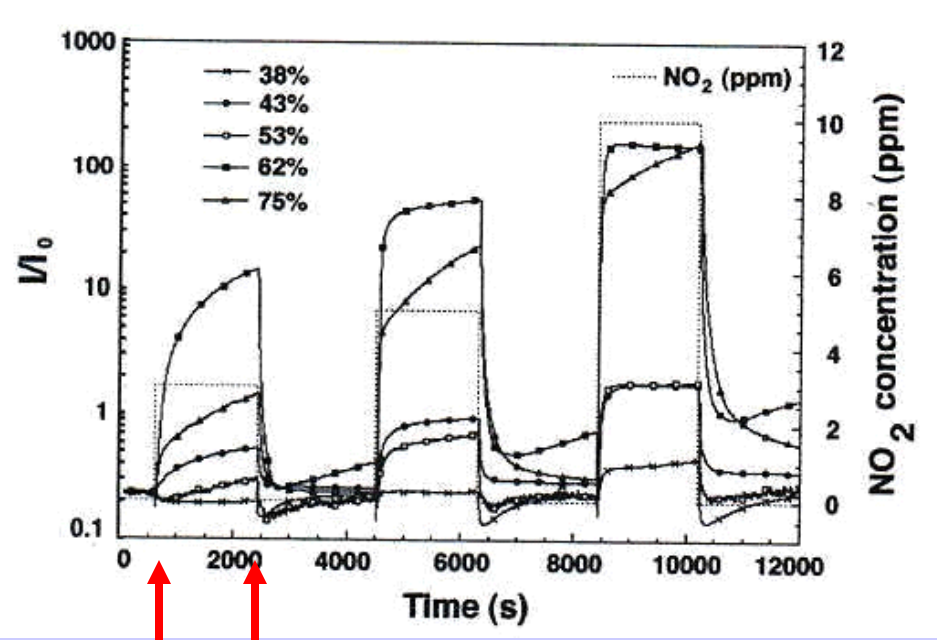

/C.Baratto, Sensors & Actuators 68(2000)74/

inlet outlet

Hydrocarbon sensors with suspended PS membrane

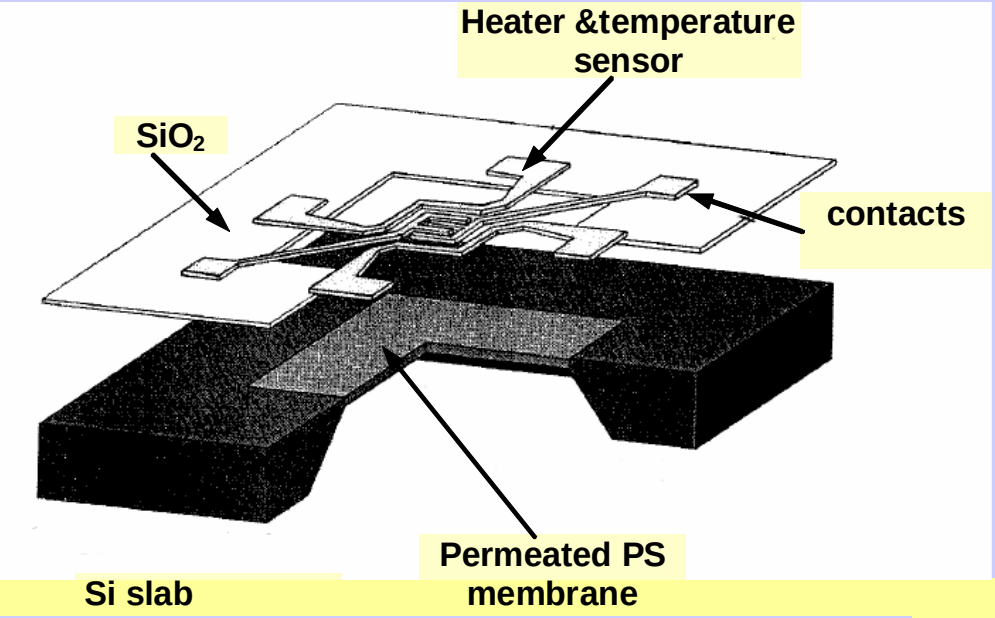

Sensitivity ΔI/I (at 0,5 ppm C_6H_6)	1,0
Response time (90 %), s	80
Recovery time (70 %), s	120
Full time for 1 cycle measurements, min	15
Cross-sensitivity (%) at 1 ppm C_6H_6, 30 ppm CO	30

$$(\Delta I_{C_2H_6+CO} - \Delta I_{CO}) / \Delta I_{C_2H_6+CO}$$

R.Angelucci, Sensors & Actuators, 74(1999)95/

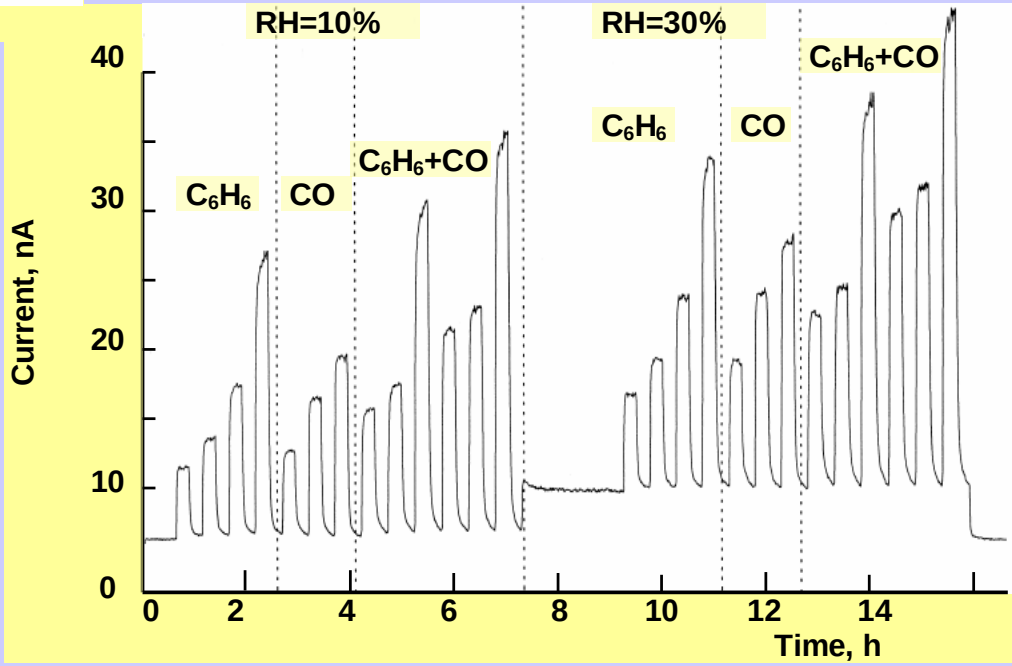

Chemical sensors (H_2) based on FET

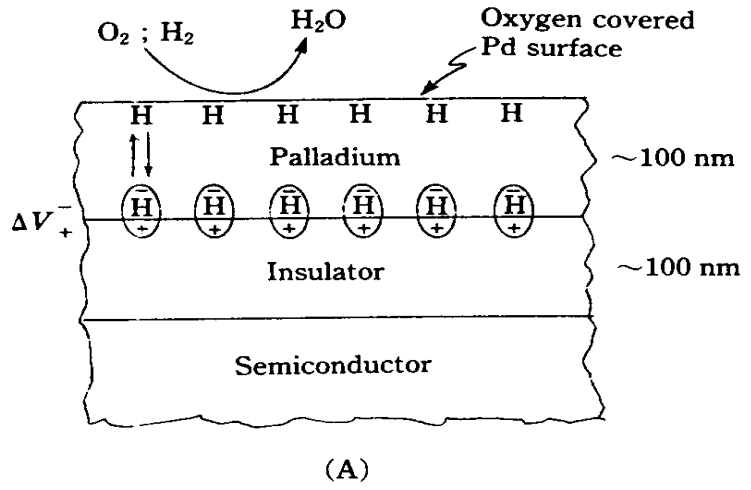

(A)

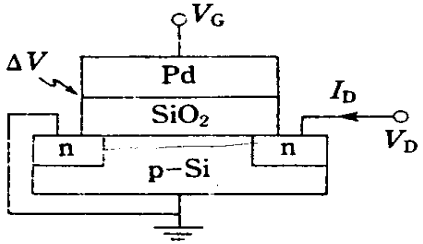

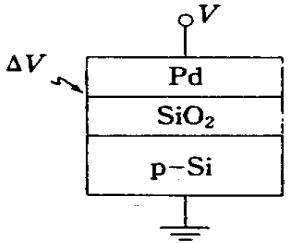

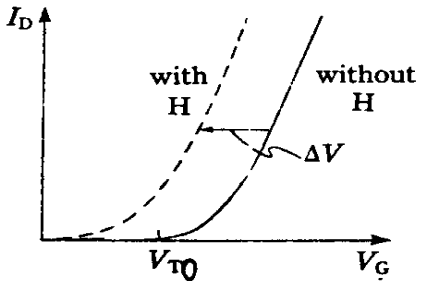

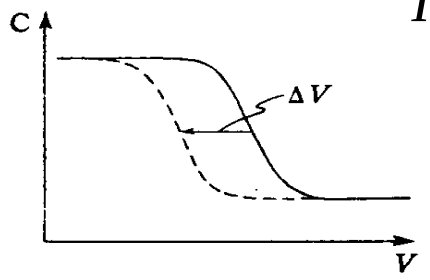

1. Hydrogen adsorption
2. Hydrogen dissociation
3. Penetration of protons through thin Pd film
4. Adsorption as dipole at Pd-SiO_2 interface

$$I_{SD} = \mu_n C_{ox} \frac{W}{L}\left[(V_G - V_T)V_{SD} - \frac{V_{SD}^2}{2}\right]$$

$V_T = V_{T0} - \Delta V$

$\Delta V = -\mu N_s \theta / \varepsilon_0$

Lundstrom I. *Sensors and Actuators*, 1 (1981) 403.

FET sensor (alcohol, acids) and capacity

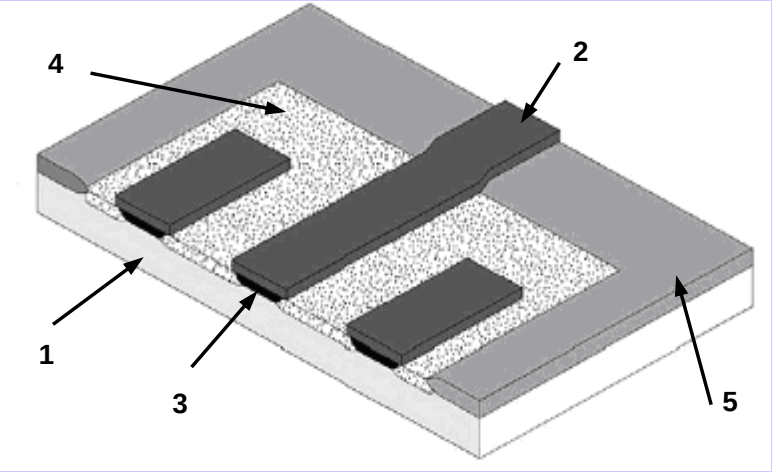

1- p-Si (10^{15} см$^{-3}$), 2- n^+ -Si, 3- impl. n-Si ($4x10^{20}$ см$^{-3}$), 4- PS, 5- Si_3N_4

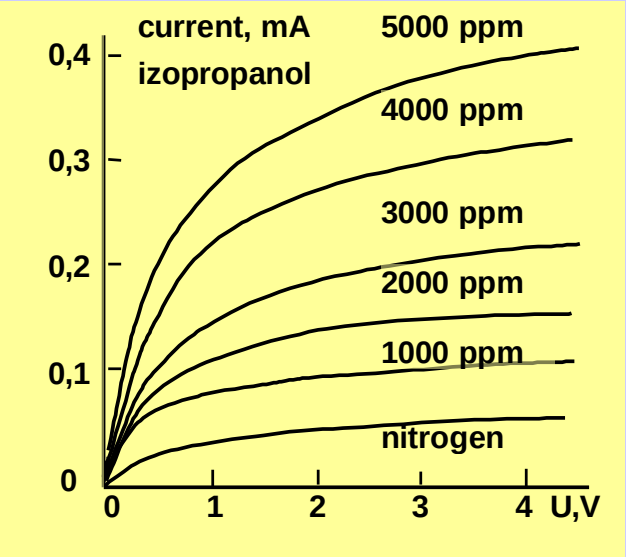

/G.Barillaro, Sensors & Actuators, 2003/

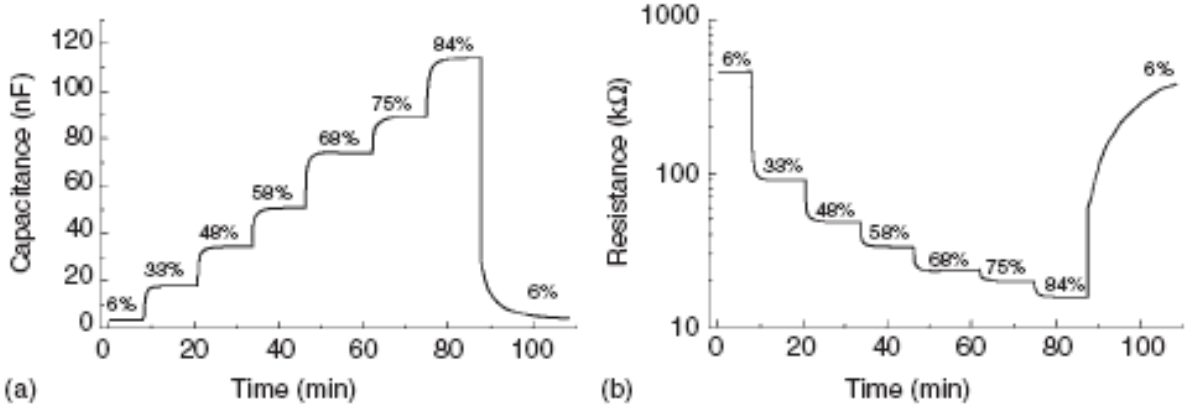

Figure 4.11 Dynamic response of (a) the capacitance and (b) the resistance of a TC-PS humidity sensor. Corresponding RH values are shown in the figures. Electrical parameters were measured using an 85 Hz frequency [58].

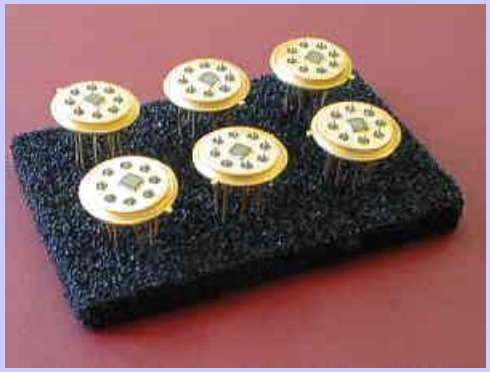

Sensor based on CMOS process

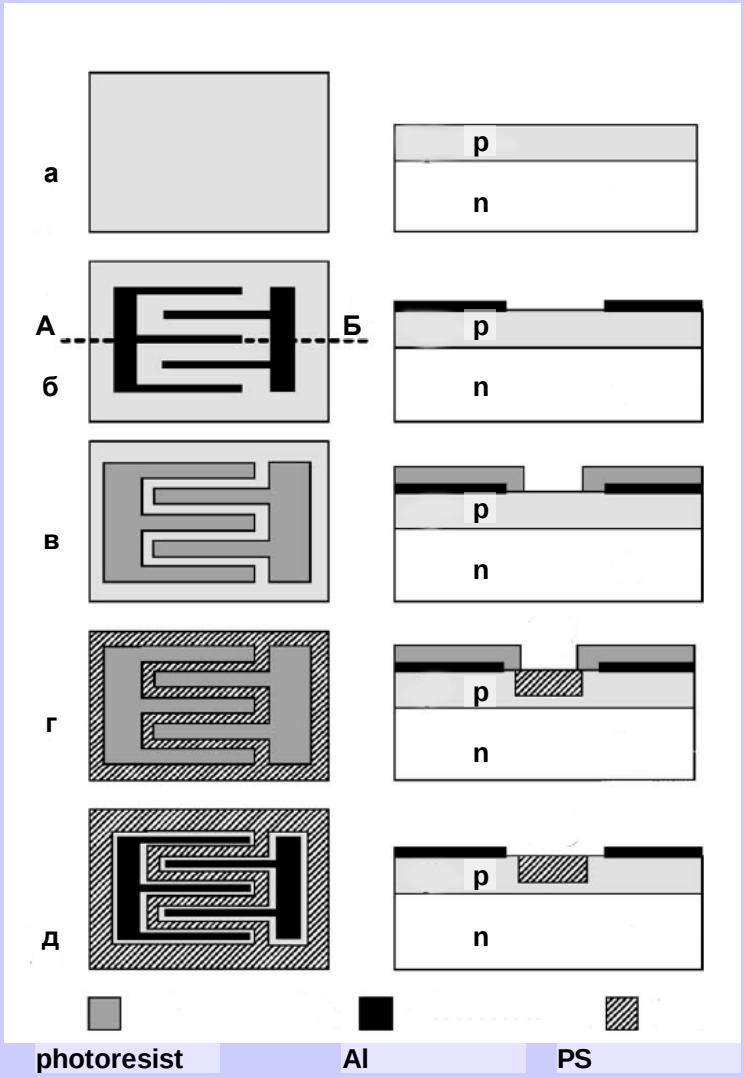

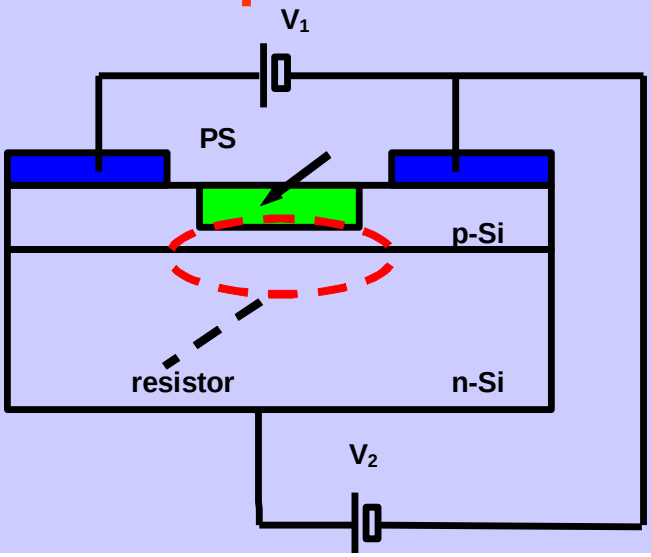

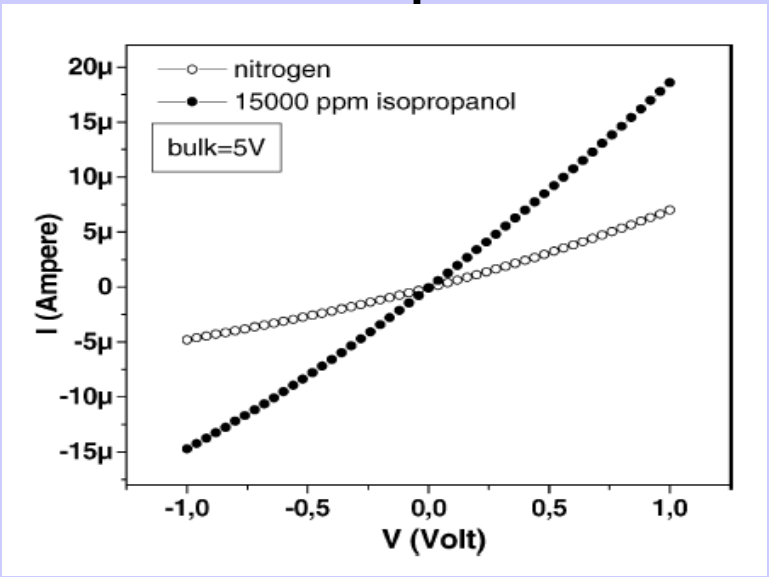

G.Barillaro, et al Sensor & Activators, B, 2004

Hydrogen storage in PS

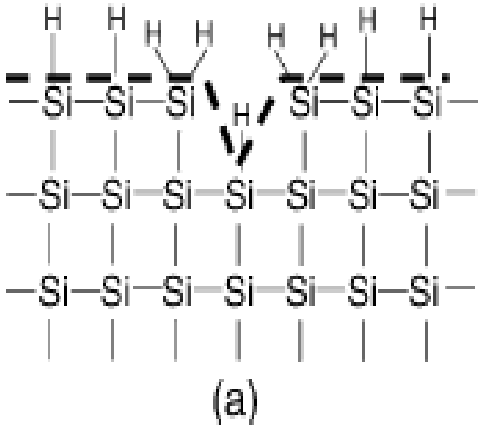

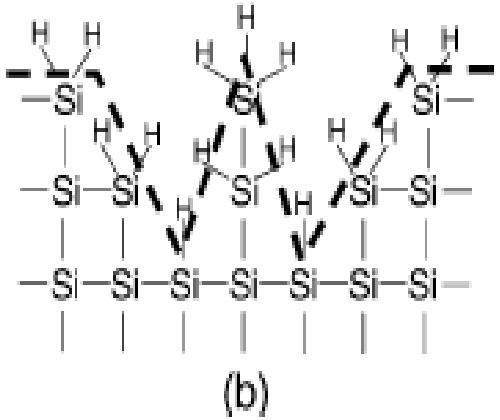

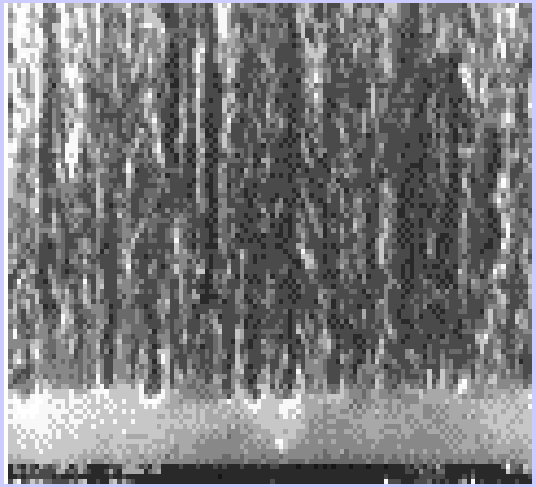

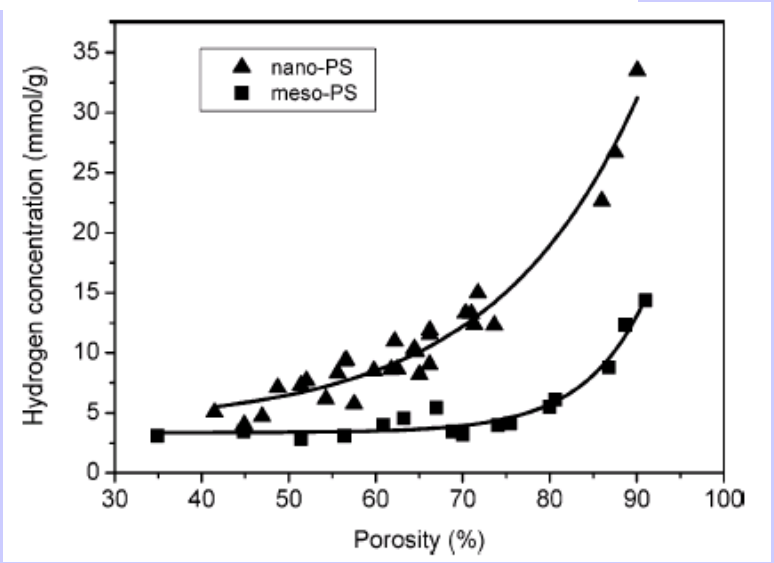

Reduction of Si nanoparticles dimension sharply increases the hydrogen concentration in PS.

Lysenko V., Barbier D., Skryshevsky V., et al., Appl.Surf.Sci., 230(2004)425

Hydrogen storage in PS

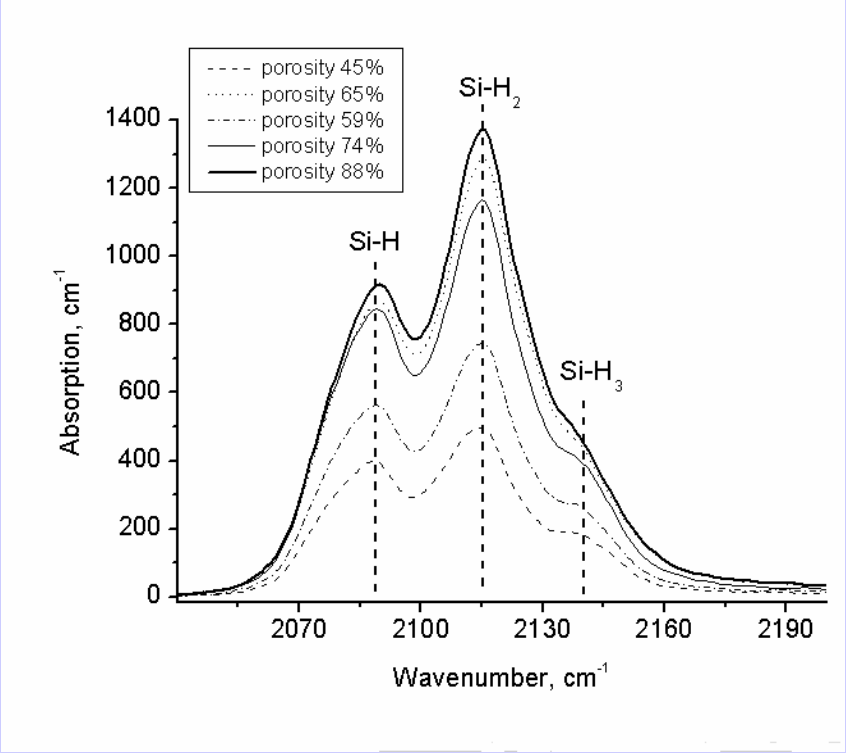

Hydrogen concentration in atomic, C_H (at.%), or mass C_M (mass%):

$$C_H = \frac{m_{Si} N_H}{1000 \rho_{Si} (1-P) + N_H (m_{Si} - m_H)}$$

$$C_M = \frac{1}{1 + \frac{m_{Si}}{m_H}\left(\frac{1}{C_H} - 1\right)}$$

$$N_H = \frac{1}{\Gamma_S \rho_{Si} (1-P)} \int_{h\upsilon} \frac{\alpha}{h\upsilon} d(h\upsilon) = \frac{I_S}{\Gamma_S \rho_{Si} (1-P)}$$

Hydrogen storage in PS

TABLE 1: Comparative Energetic Analysis of PS Nanostructures for Their Application as Hydrogen Reservoirs in Portable Devices

materials	atomic hydrogen content, (mmol g^{-1})	theoretical mass energy density, (W-h kg^{-1})	autonomy (h) of a device consuming 1 W and using 100 g of material storing hydrogen *(taking into account 50% efficiency of low-temperature fuel cell)*
meso-PS (90%, 10 nm)	13	429	21.4
nano-PS (90%, 5 nm)	34	1120	56.1
nano-PS powder (>95%, 2–3 nm)	66	2176	108.8
reversible metal hydrides[4]			
$MgH_2 \rightarrow Mg + H_2$	76	2505	125.2
$LaNi_5H_6 \rightarrow LaNi_5 + 3H_2$	14	461	23
hydride hydrolysis[4]			
$(NaBH_4 + 2H_2O) \rightarrow NaBO_2 + 4H_2$	108	3560	178
$(LiBH_4 + 4H_2O) \rightarrow LiOH + H_3BO_3 + 4H_2$	85	2802	140.1
hydride thermolysis[4]			
$NH_4BH_4 \rightarrow BN + 4H_2$	244	8043	402.1
$NH_3BH_3 \rightarrow BN + 3H_2$	195	6428	321.4
methanol reforming			
$(CH_3OH + H_2O) \rightarrow CO_2 + 3H_2$	120	3956	197.8
Li-ion batteries [24][5]			
(for comparison)		150	15

2 mmol/g (H_2, 60% porosity)
3,7 mmol/cm^{-3} (H)

(Rivolo et al., Phys. Stat. Sol. (a) 197, (2003) 217)

Nano-porous powder, nanocrystallite dimension - 2nm

66 mmol/g H

Thermally stimulated desorption

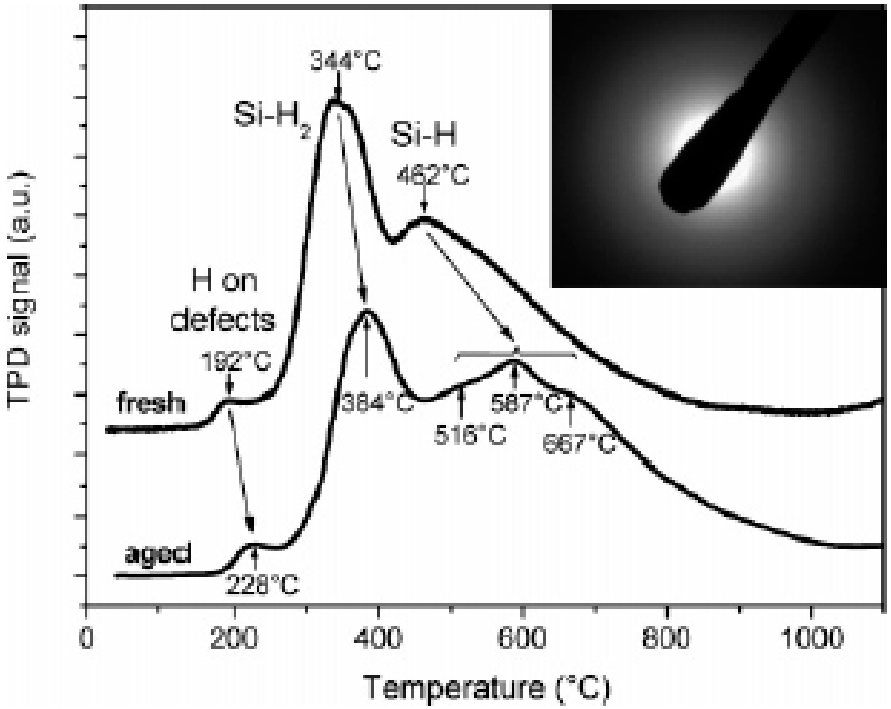

Figure 6. Effusion curves for H_2 desorption from fresh and aged nano-PS samples. Electron diffraction image given in insert reflects amorphous structure of the PS samples.

V.Lysenko, et.al. J.Phys.Chem., B, 2005, 109, 19711

Chemically stimulated desorption

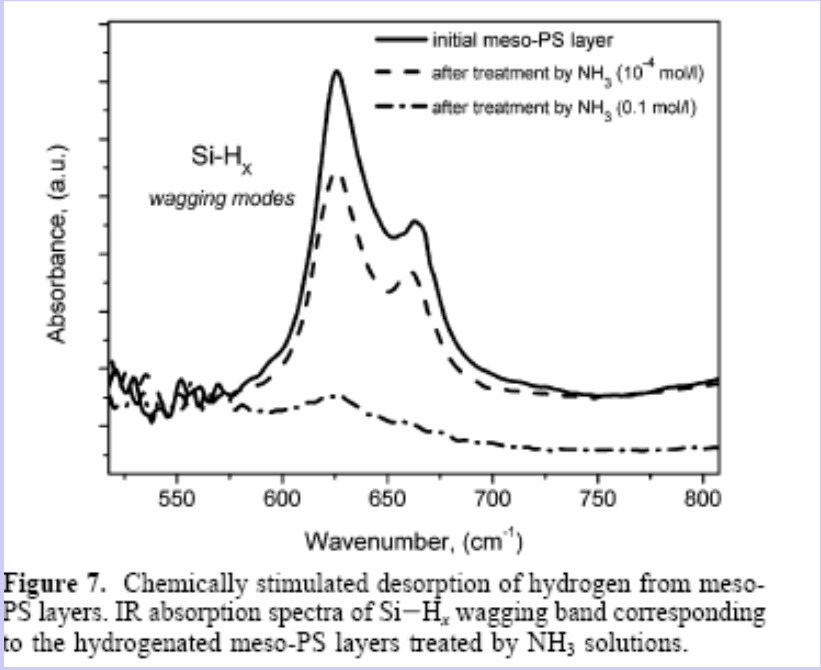

Figure 7. Chemically stimulated desorption of hydrogen from meso-PS layers. IR absorption spectra of $Si-H_x$ wagging band corresponding to the hydrogenated meso-PS layers treated by NH_3 solutions.

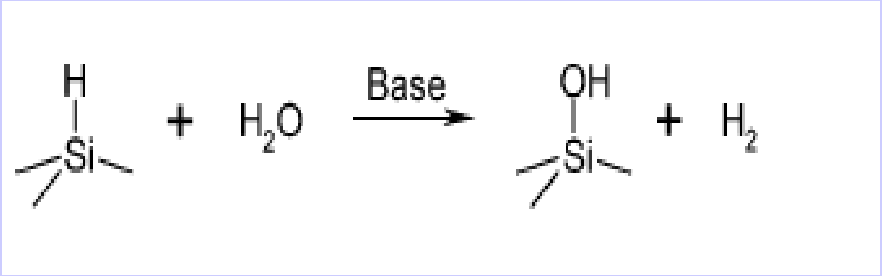

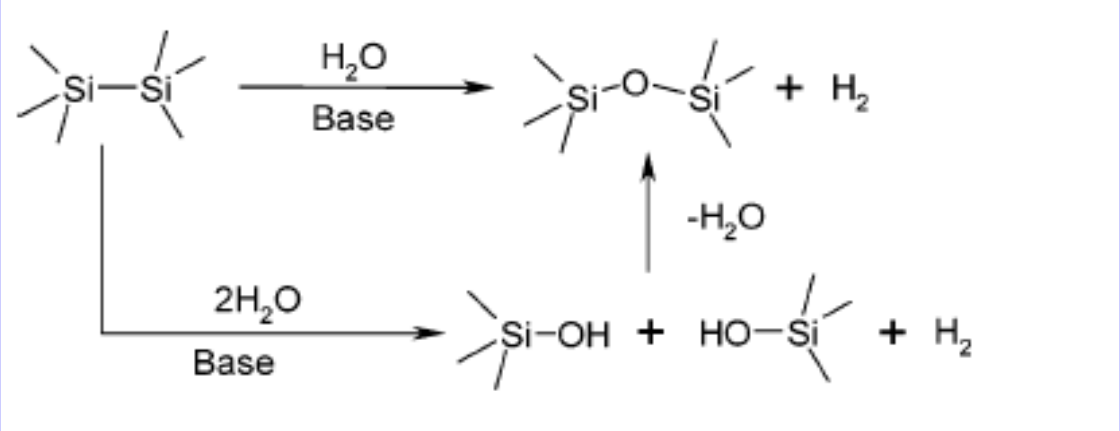

Chemically stimulated desorption

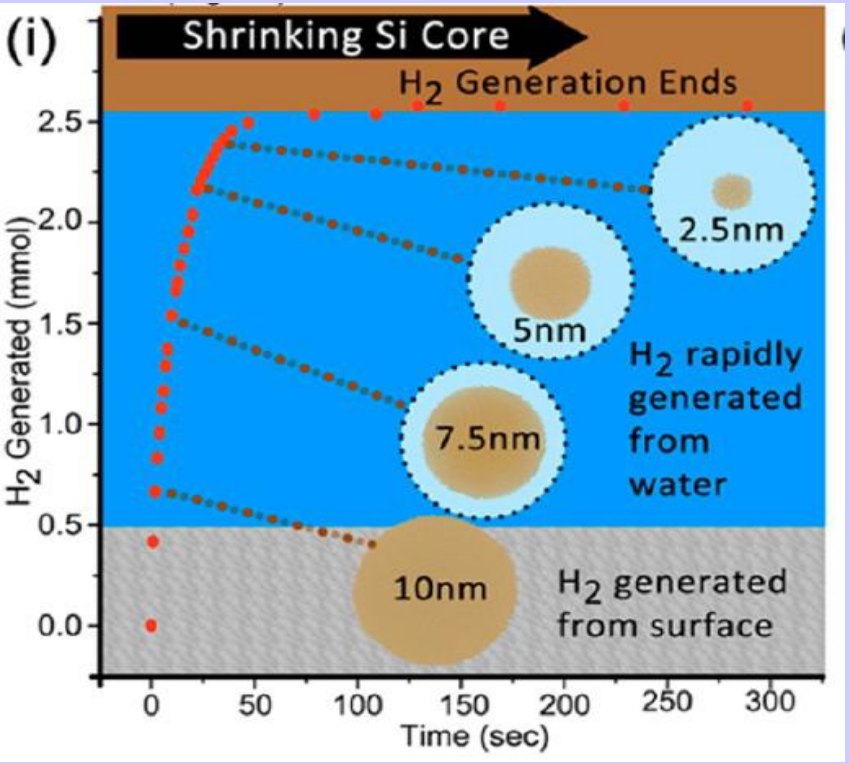

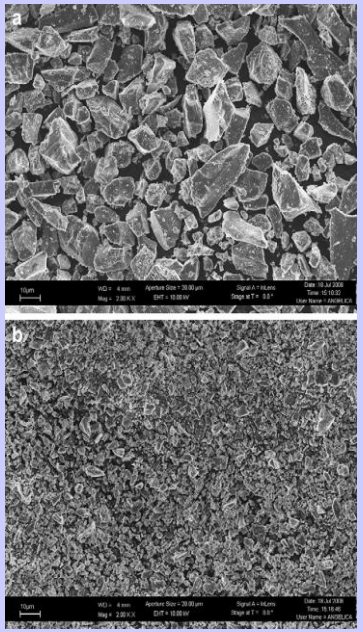

Conceptual illustration of a shrinking core model that describes H_2 generation from 10 nm Si NP. Brown spheres represent NPs, and the dotted circle indicates shrinkage from the original sphere size. The gray and blue areas represent hydrogen contributed by the silicon and by water, respectively

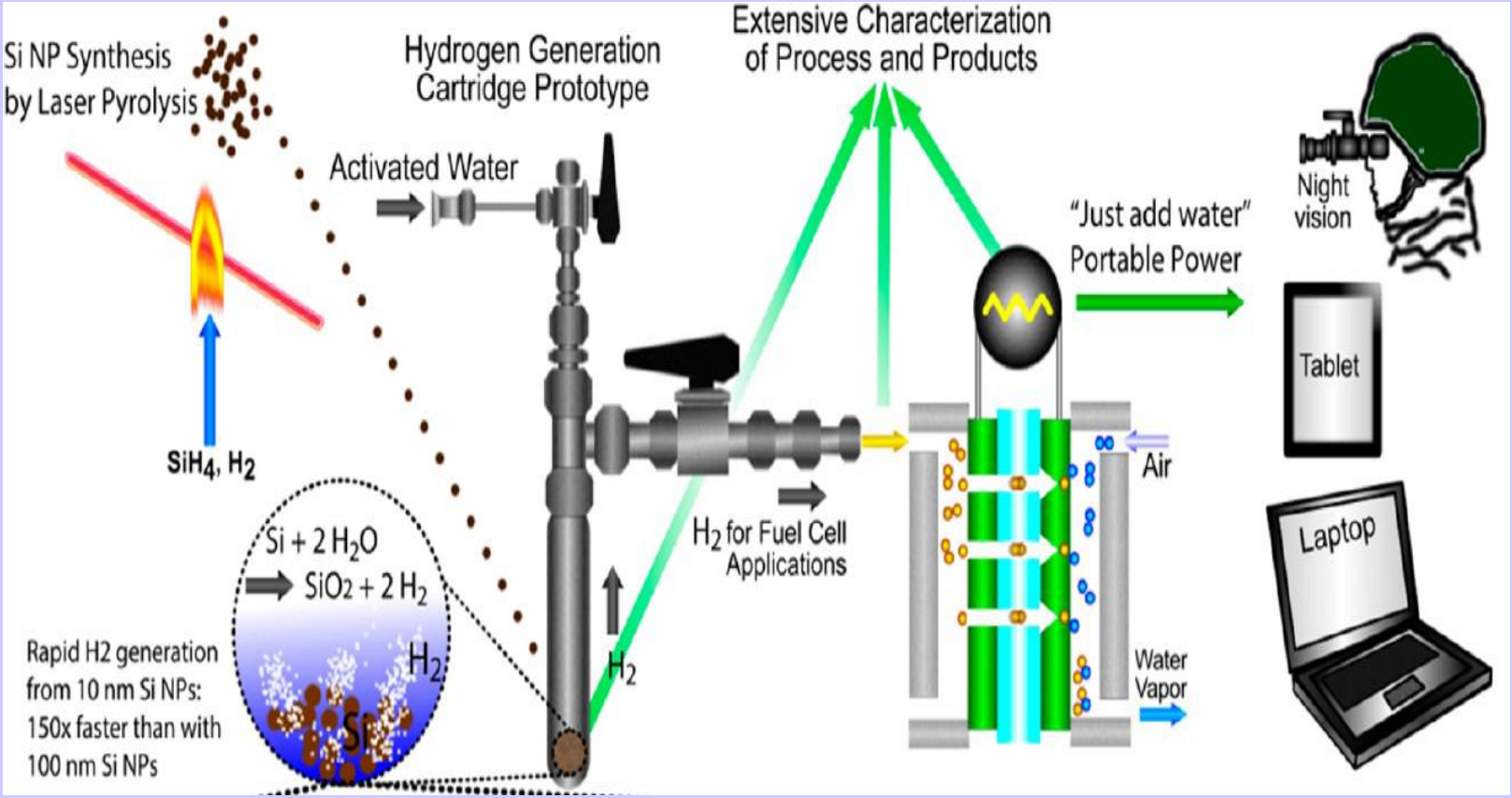

Schematic showing CO_2 laser pyrolysis synthesis of silicon nanoparticles transferred to a custom stainless steel prototype cartridge used to generate hydrogen for fuel cell applications

Erogbogbo, F. et al. On-demand hydrogen generation using nanosilicon: splitting water without light, heat, or electricity. Nano Lett. 13, 451–456 (2013).

Portable energy supply

+ 10g of nano-porous *(6.6 wt%)*

11 hours of autonomy
(Li battery: 1 hour)

V.Lysenko, private commun.

Thermal isolation

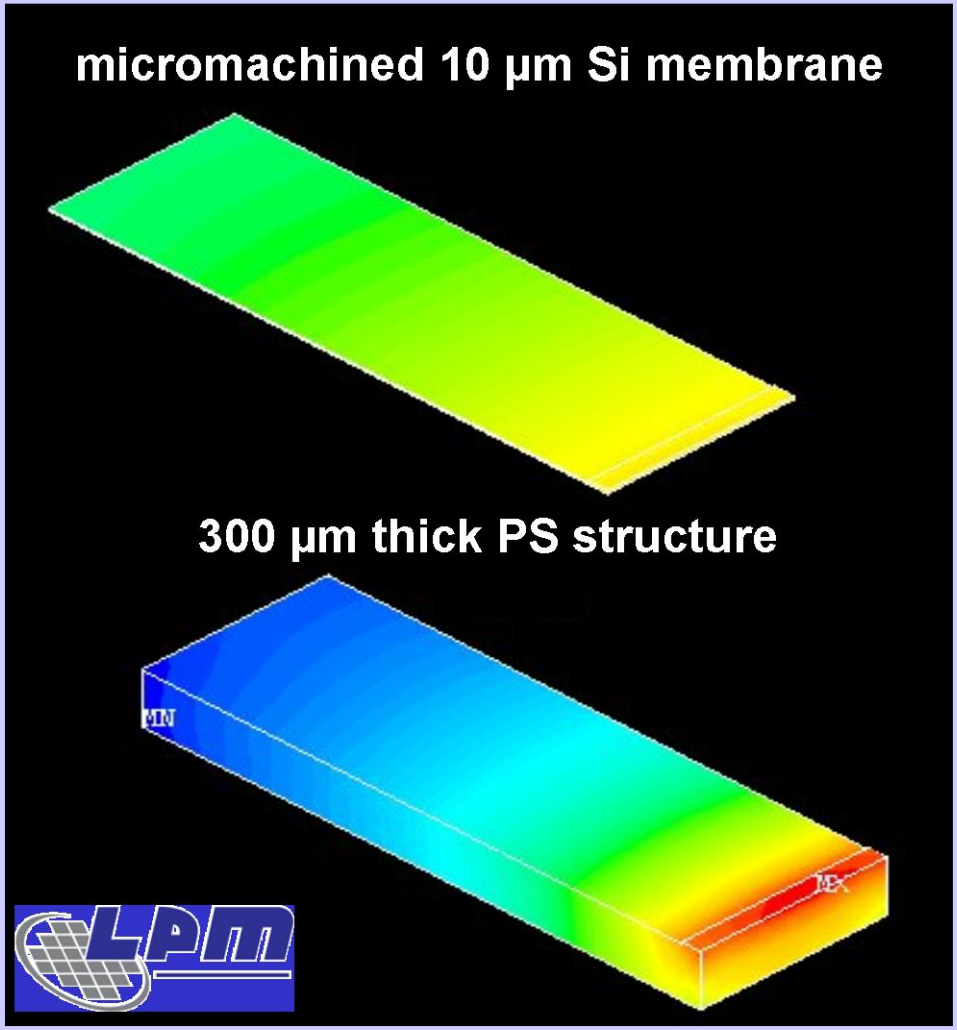

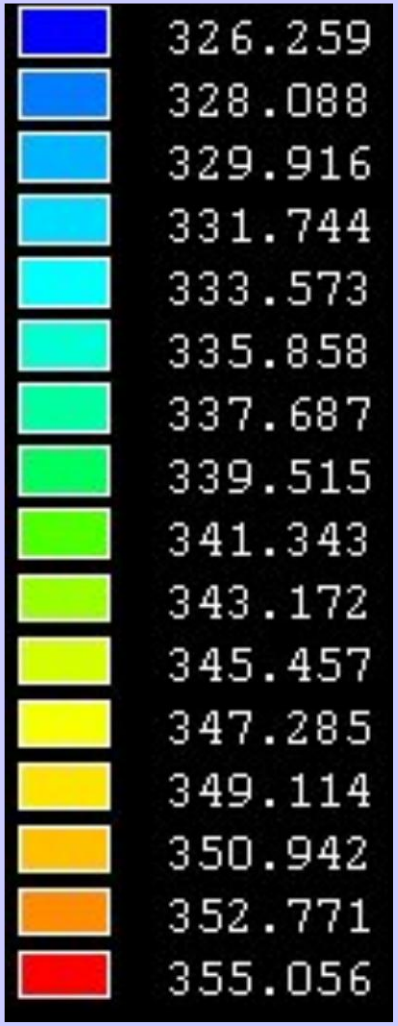

Explosive reactions

- Conditions: H-terminated porous Si surface + liquid oxygen
- 3 step chain mechanism : a) oxidation of Si dangling bonds (10^{16} cm^{-3});
  b) rupture of Si-H bonds;
  c) $2H_2+O_2=2H_2O$ ...

- Energy yield : 12- 28 kJ/g
  (trinitrotoluene : 4.2 kJ/g)
- Explosion time : $2x10^{-7}$ s
- Velocity of the reaction front propagation : 10^4 m/s
- Shock wave pressure : 11 GPa/cm^2

Kovalev et al., Phys. Rev. Lett. 87, (2001) 068301

Table 19.2 Overview of some thermodynamic reaction parameters for several mixtures of Si with oxidizer.

Chemical reaction equations	ΔH_r^0 (kJ)	ΔH_r^0 (kJ/g)	T_{rct} (K)
$Si + O_2 \rightarrow SiO_2$	−911	−15.2	3131
$4Si + Ca(ClO_4)_2 \rightarrow 4SiO_2 + CaCl_2$	−3703	−10.5	3093
$2Si + NaClO_4 \rightarrow 2SiO_2 + NaCl$	−1850	−10.4	3057
$2Si + KClO_4 \rightarrow 2SiO_2 + KCl$	−1825	−9.4	3061
$5Si + 4NH_4ClO_4 \rightarrow 5SiO_2 + 2N_2 + 4HCl + 6H_2O$	−5453	−8.9	2917
$5Si + 4NaNO_3 \rightarrow 5SiO_2 + 2N_2 + 2Na_2O$	−3519	−7.3	2893
$5Si + 4KNO_3 \rightarrow 5SiO_2 + 2N_2 + 2K_2O$	−3305	−6.1	2980
$4Si + S_8 \rightarrow 4SiS_2$	−848	−2.3	1759
$nSi + (C_2F_4)_n \rightarrow nSiF_4 + 2nC$	−798	−6.2	3532

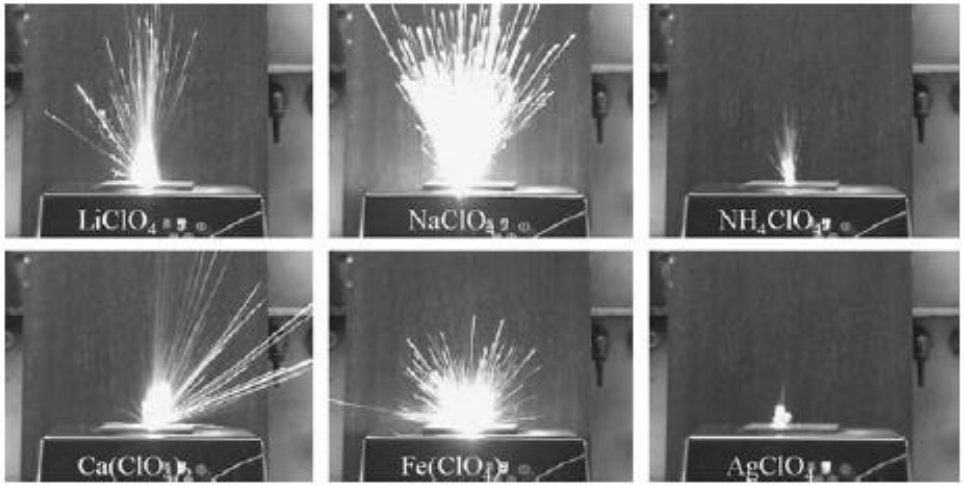

Figure 19.14 Time-integrated flame pictures of 3 × 3 mm PSi single elements filled with the indicated oxidizers (this image was prepared by D. Clément, Technical University of Munich, for the "SilAnz" report [14]).

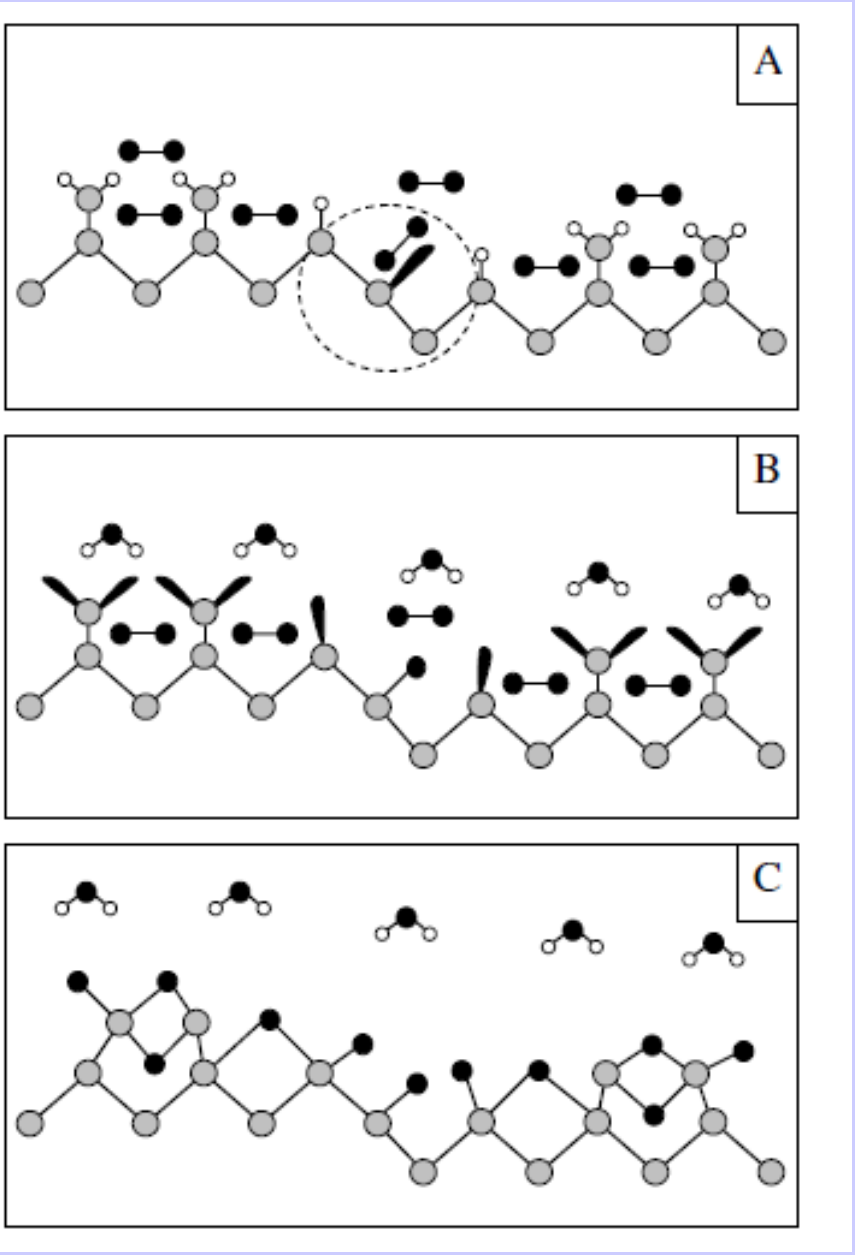

Three principal steps of the explosive reaction of oxygen (black circles) with hydrogenated PS open circles are hydrogen atoms, gray circles are silicon atoms, black lobes are Si dangling bonds)

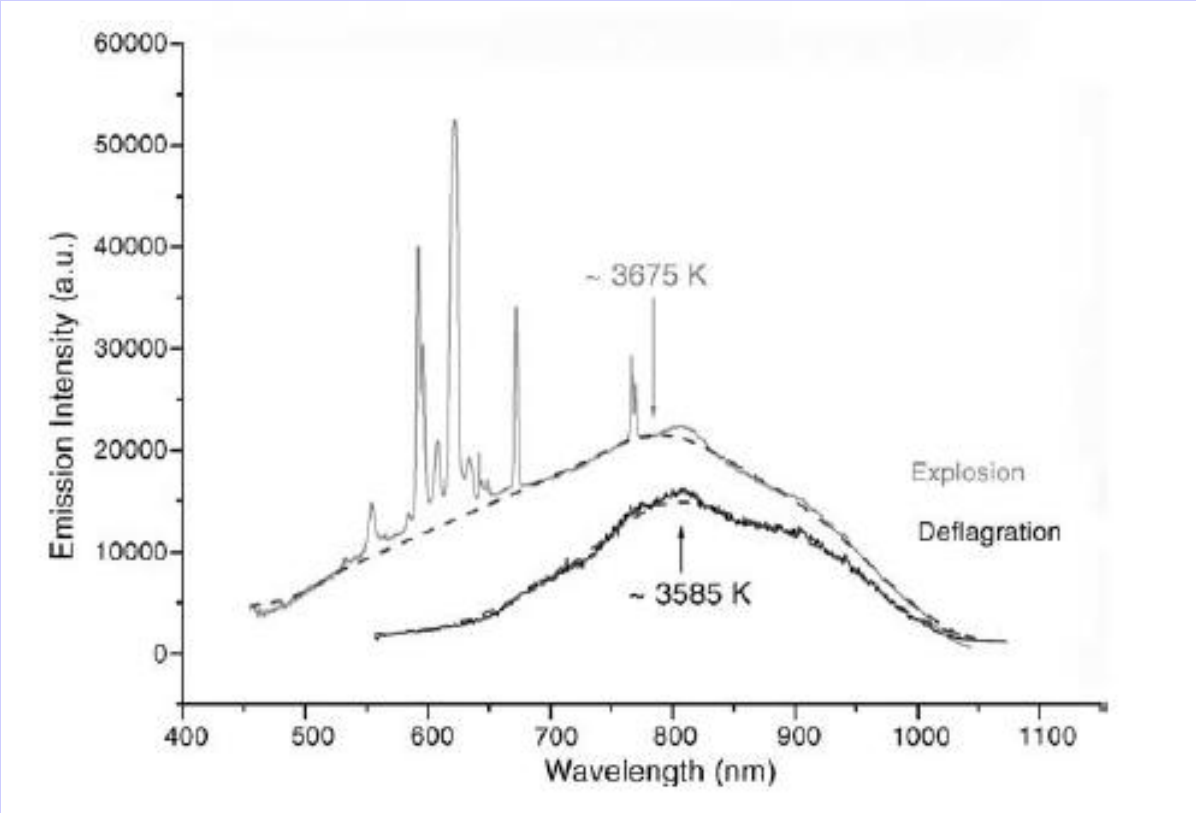

Figure 19.13 Emission spectra of flashes accompanying the explosions. The reaction temperatures are indicated and were estimated by the approach of a blackbody emission. They are very similar for the deflagration and the explosion. The spectrum of the explosion additionally shows the appearance of plasma lines of single or double ionized atoms demonstrating the presence of hot spots having temperatures much higher than the estimated ones (this image was prepared by D. Clément, Technical University of Munich, for the "SilAnz" report [14]).

Biosilicon ™

(pSi Medica Ltd., Prof. L. Canham)

"Intelligent" tablets releasing the drugs when and where they are needed.

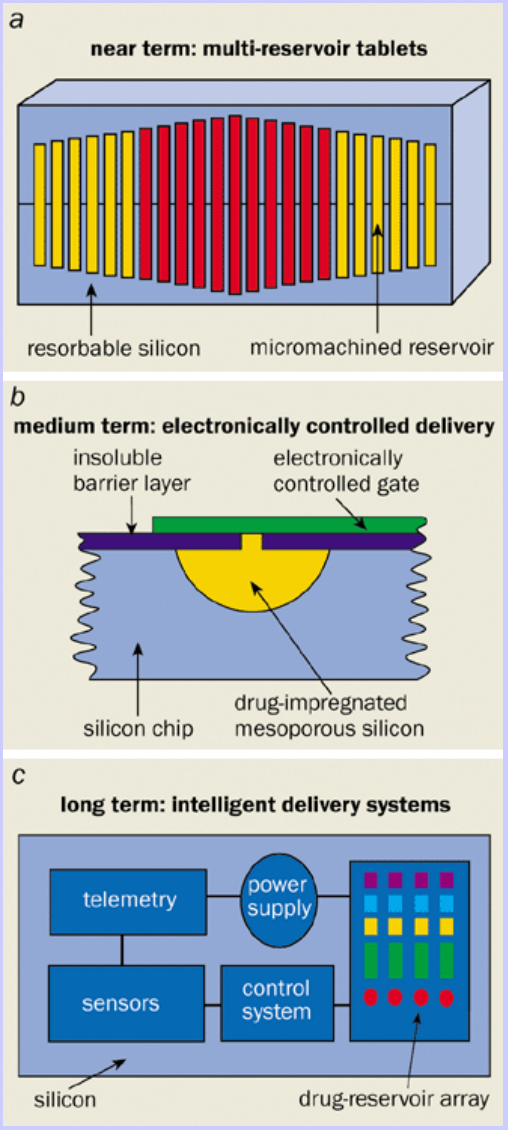

Model of unsolube molecule delivery with magnetic nanoparticles in porous silicon

Figure 1 Tiny reactors. Drops of aqueous solutions of Ag^+ and I^- in dichloromethane are coated with a self-assembled layer of magnetic porous silicon crystals. The droplets are transported with magnets towards each other. When they meet they coalesce to form a new, larger droplet. The precipitation of insoluble AgI takes place immediately inside the newly merged aqueous drop.

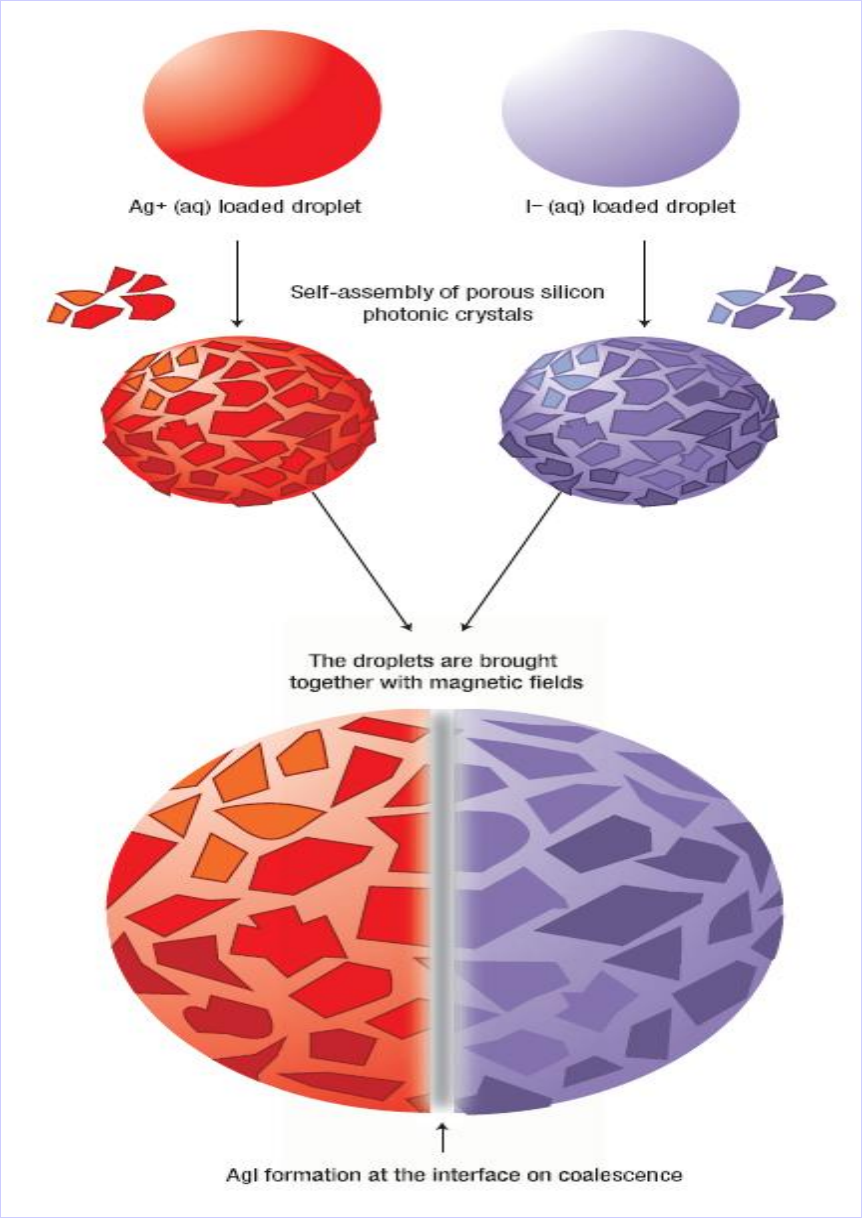

J.Buriak, Nature materials, 3, 2004, 847

Drug delivery with magnetic nanoparticles in porous silicon

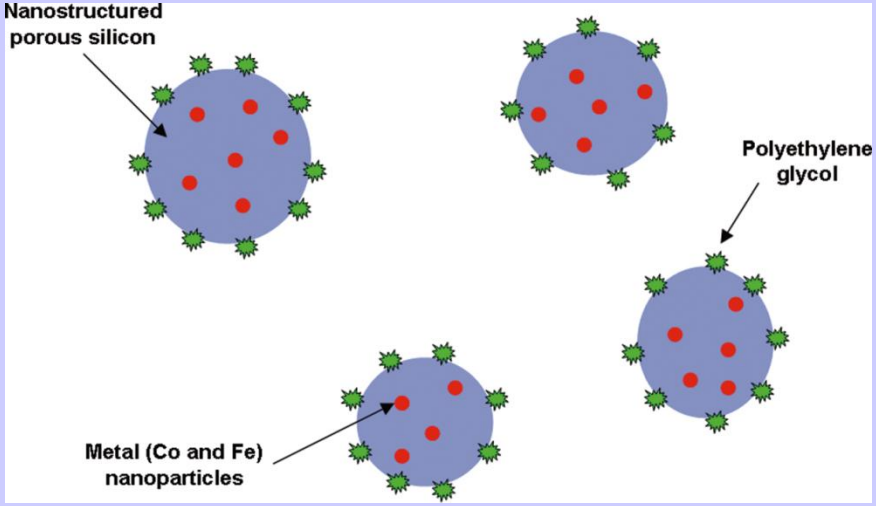

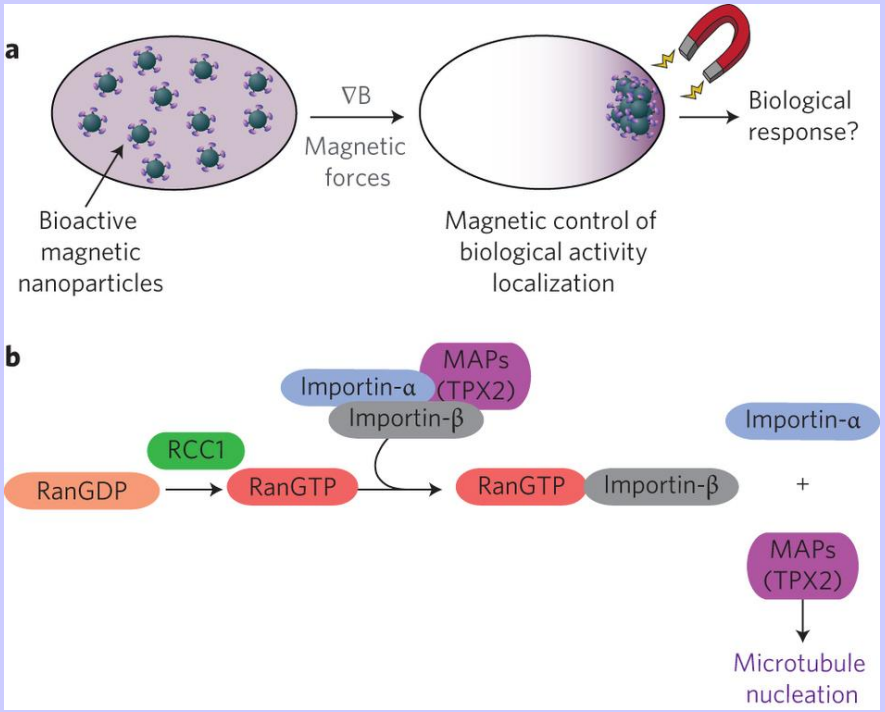

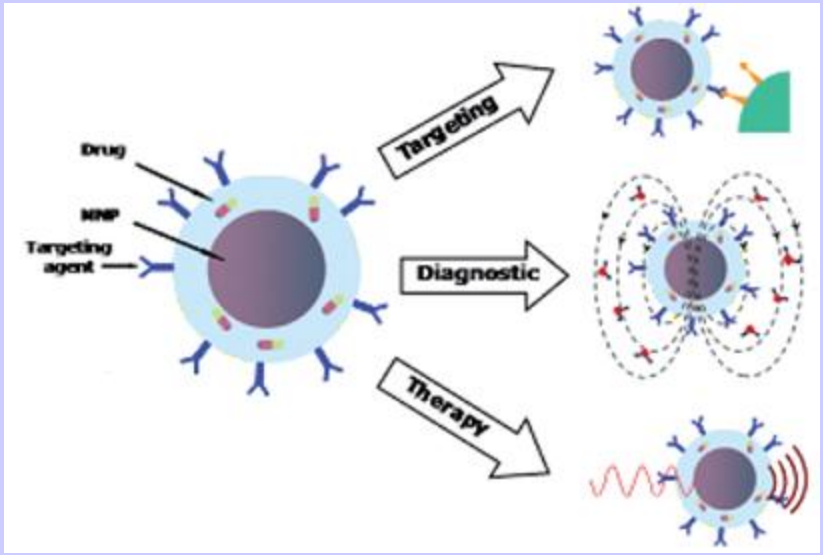

Semiconductor Nanoparticles for cell imaging

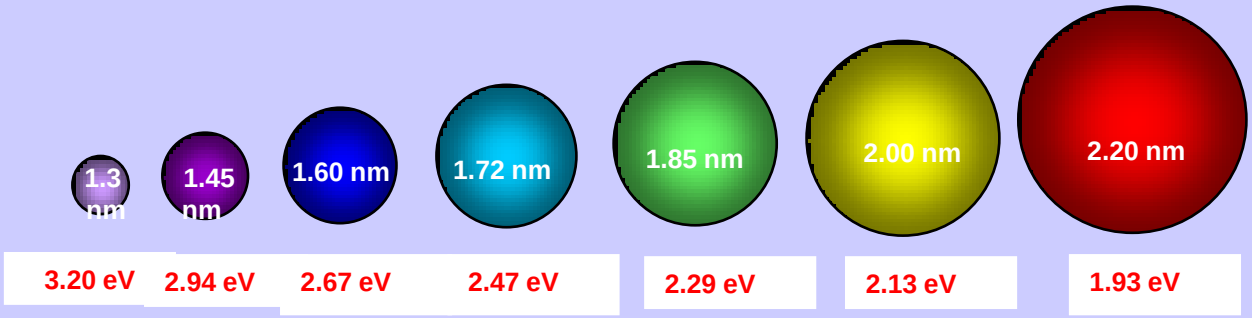

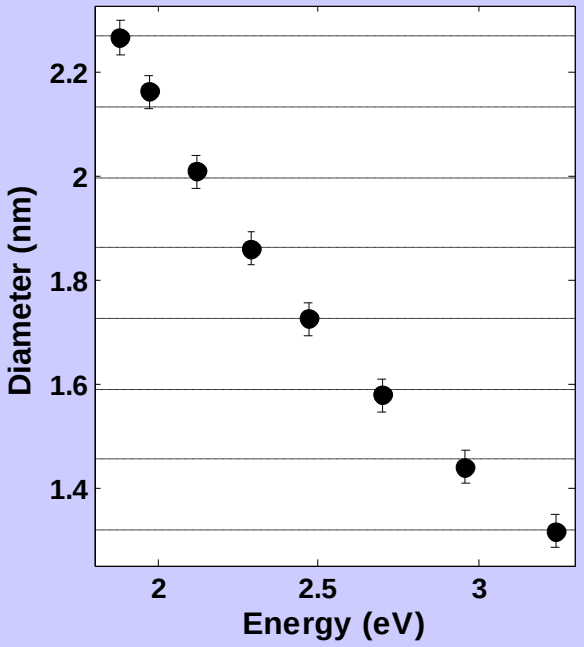

J.K. Jaiswal, S. M. Simon, *Trends in cell biology*, vol 14, 497-504 (2004)

Water-dispersed Si/SiO_xH_y core/shell QDs with a Si core of different controlled diameters

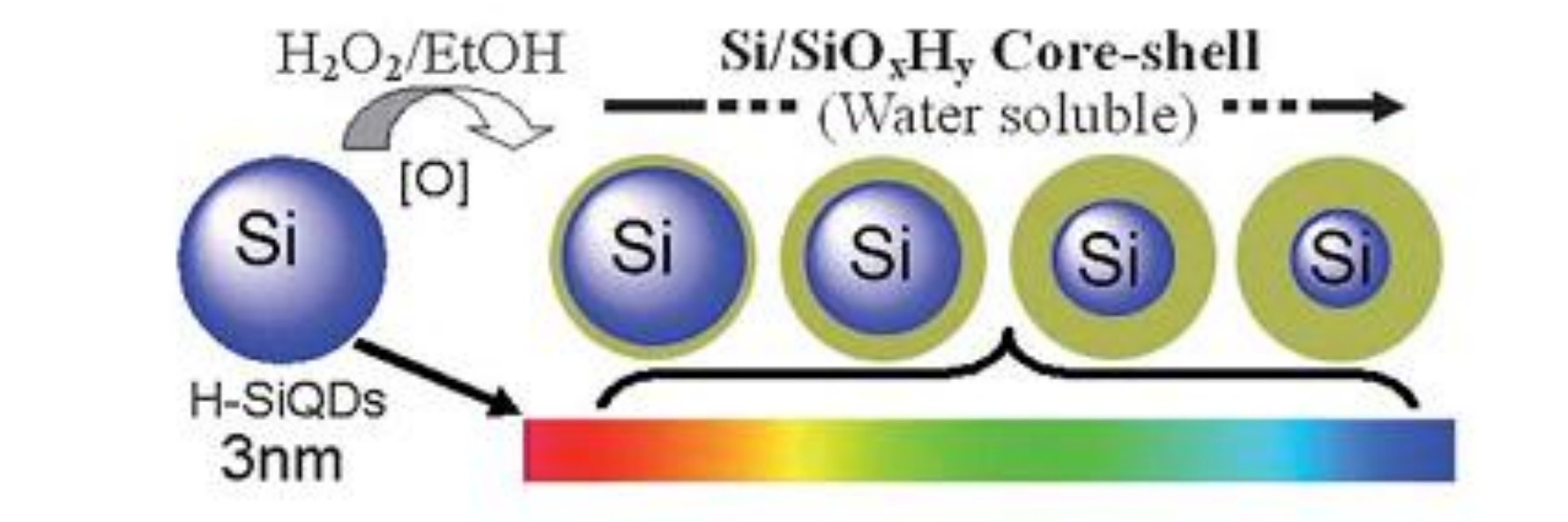

3 nm H-SiQDs are oxidized in EtOH–H_2O_2; emission of the oxidized SiQDs ranges from salmon pink to blue

Kang ZH, et al. (2009) , Adv. Mater. 21: 661-664

Images of organs of a Balb C mouse

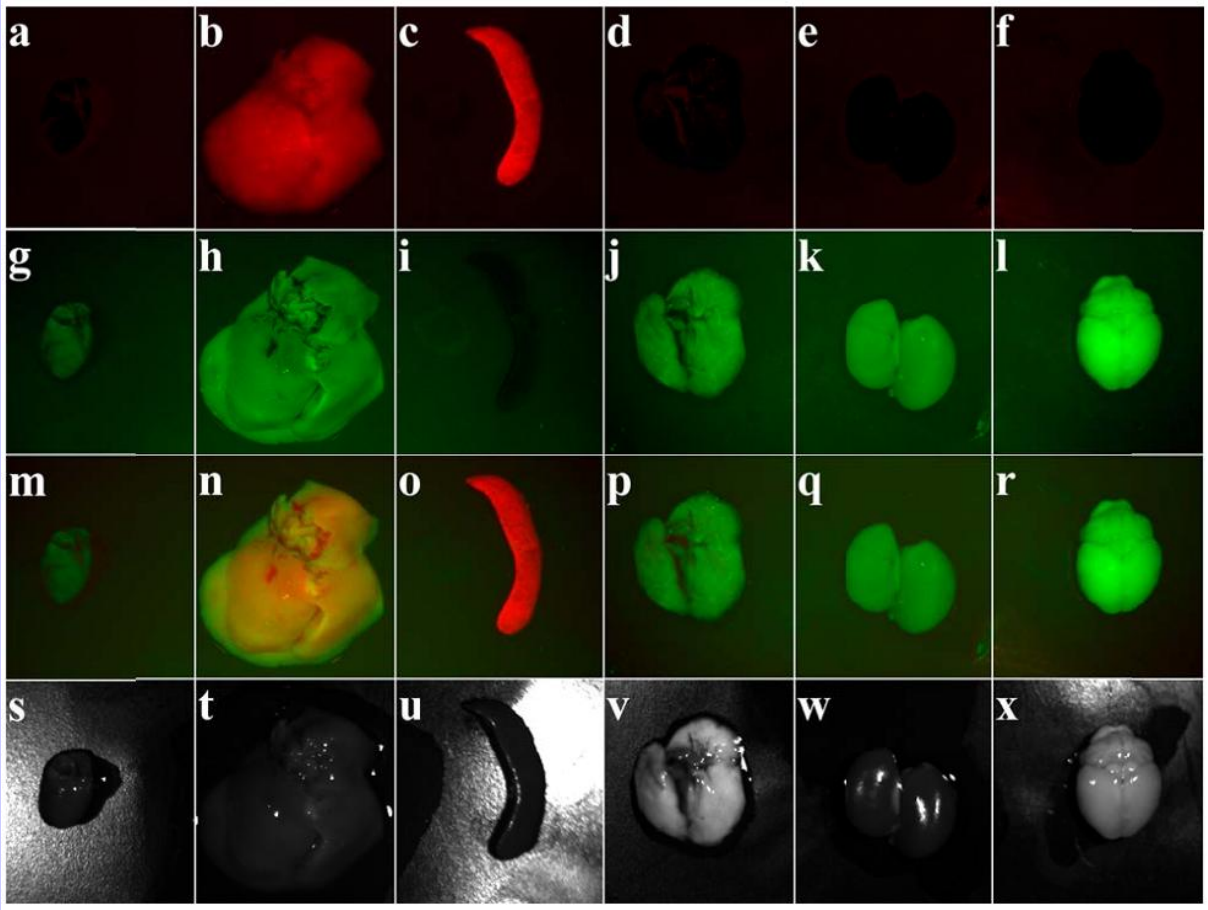

Images of organs of a Balb C mouse 24 hours after injection of the PSiQDs. A, G, M, S: **Heart**; B, H, NN, T**: Live**r; C, I, O, U: **Spleen**; D, J, P, V: **Lungs**; E, K, Q, W: **Kidneys**; F, L, R, X: **Brain**. Top Row: Fluorescence; Second Row: Autofluorescence; Third Row: Overlay; Fourth Row: White light picture

May J L, Erogbogbo F, et al. Journal Solid Tumors. 2012, 2: 24-3

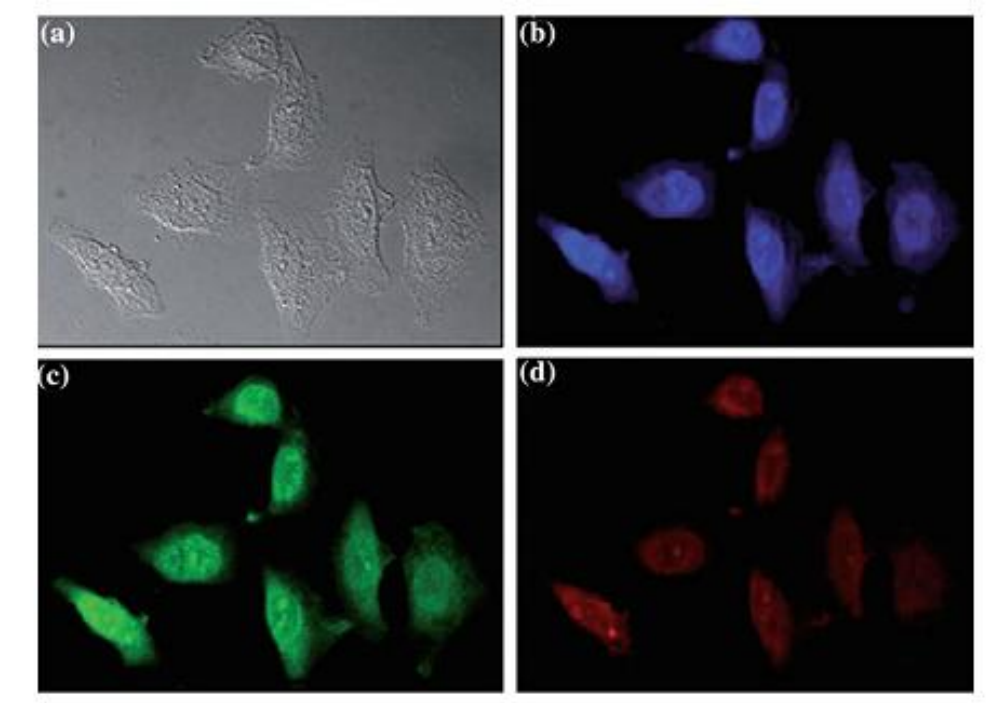

Confocal microscopic visualisation of HeLa cells treated with carboxylic acid terminated Si QDs collected at different channels: a) bright field image; and luminescence images collected at: b) 450 nm, c) 515 nm, and d) 605 nm

HeLa — линия «бессмертных» клкток, (они способны делиться бесконечное число раз) используемая в научных исследованиях. Была получена в1951 из раковой опухоли шейки матки

Liu W, (2011), Chem. Eur. J. 17: 12872 – 12876

General rule of analyte determination based on QD fluorescence emission quenching

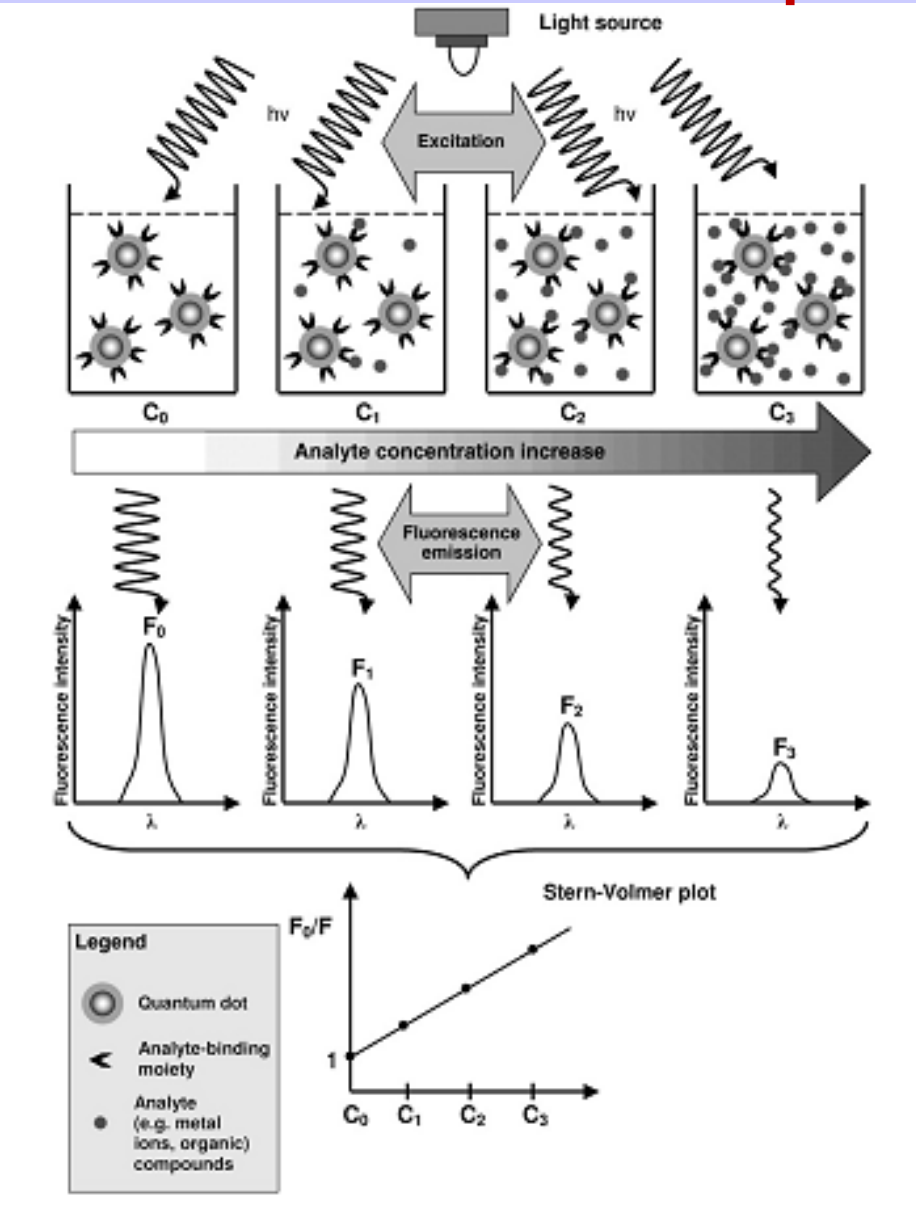

M.Geszke-Moritz, et al, Mater.Sci.Eng.C 33 (2013) 1008

Label-free Si QDs as PL probes for glucose detection

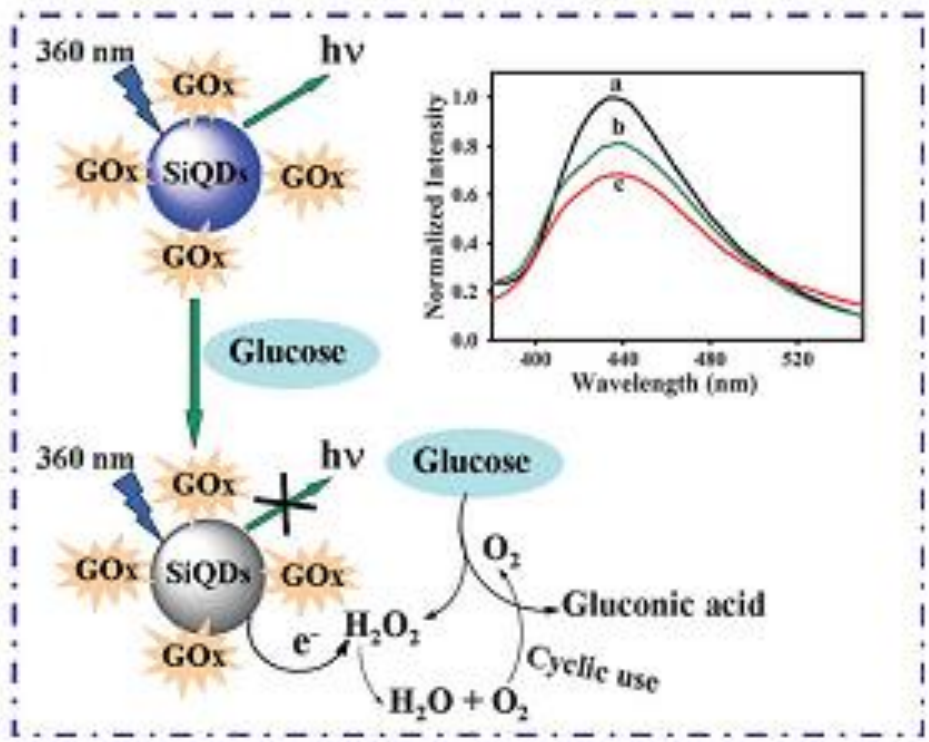

Schematic illustration of the glucose sensor based on H_2O_2 -sensitive SiQDs.
Inset: the normalized PL spectra of SiQDs in solution in the absence (a) and presence of 0.5 mM H_2O_2 (b) and 0.5 mM glucose containing 10 μg mL GOx (c) in PBS (pH 7.4) for 30 min.

$$\text{Glucose} + O_2 + H_2O \xrightarrow{(GOx)} \text{gluconic acid} + H_2O_2$$

Yinhui Yi et al, Chem. Commun., 2013, 49, 612--614

SiC QDs in colidal solutions

No oxidation in water of SiC nanoparticles!

a) Highly porous 3C- SiC layer, b) 3C- SiC nanopowder, c) colloidal solution with dispersed 3C- SiC QDs

Yu. Zakharko, J. Botsoa, S. Alekseev, V. Lysenko, J.-M. Bluet, O. Marty, V.Skryshevsky, G. Guillot,*J.Appl.Phys*, 107, 013503, 2010

SiC QDs as a contrast and fluorescent agent for animal cells imaging

FIBROBLAST CELLS

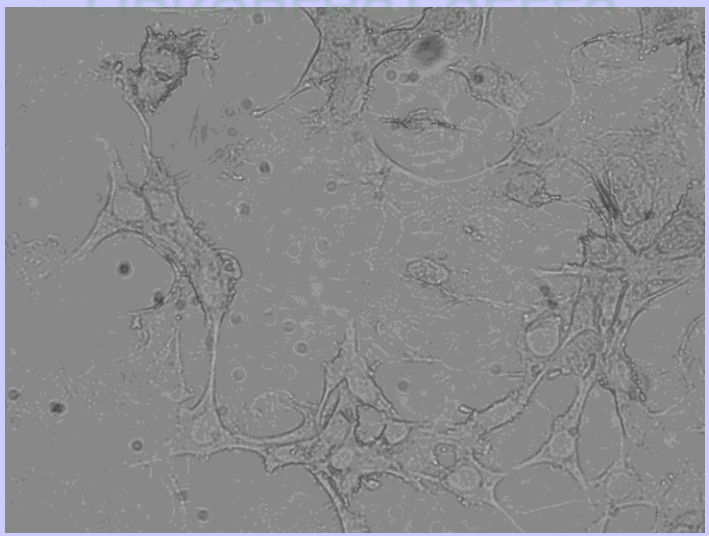

FIBROBLAST CELLS WITH SIC QDS

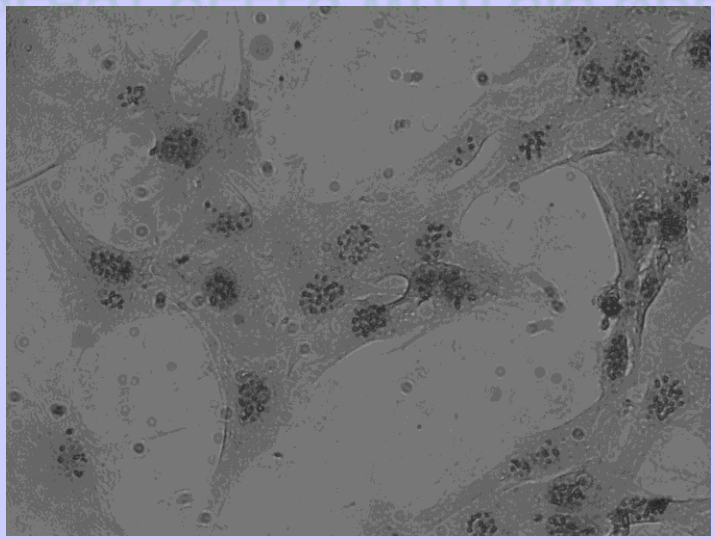

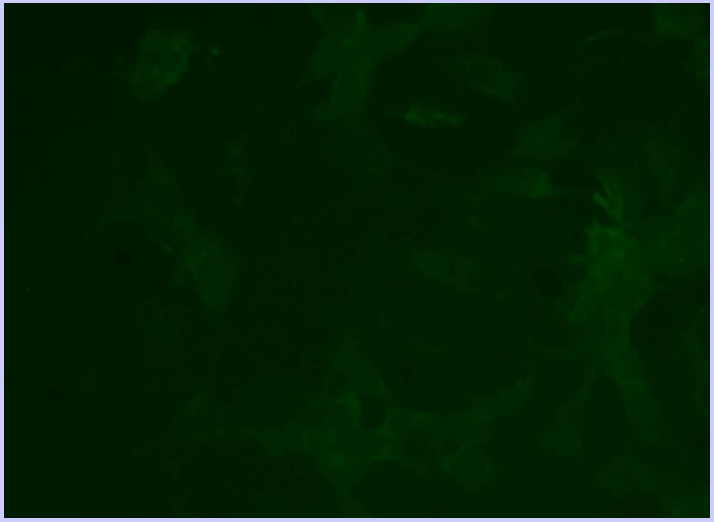

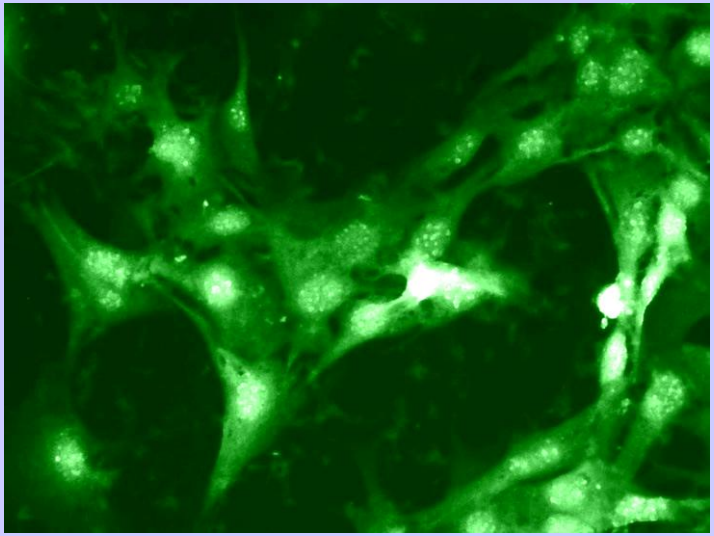

Impact of cell division on intracellular uptake and nuclear targeting with fluorescent SiC-QDs

SG (healthy) epithelian human cells

HSC (cancer) epithelian human cells

Low confluence

Medium confluence level

Full confluence

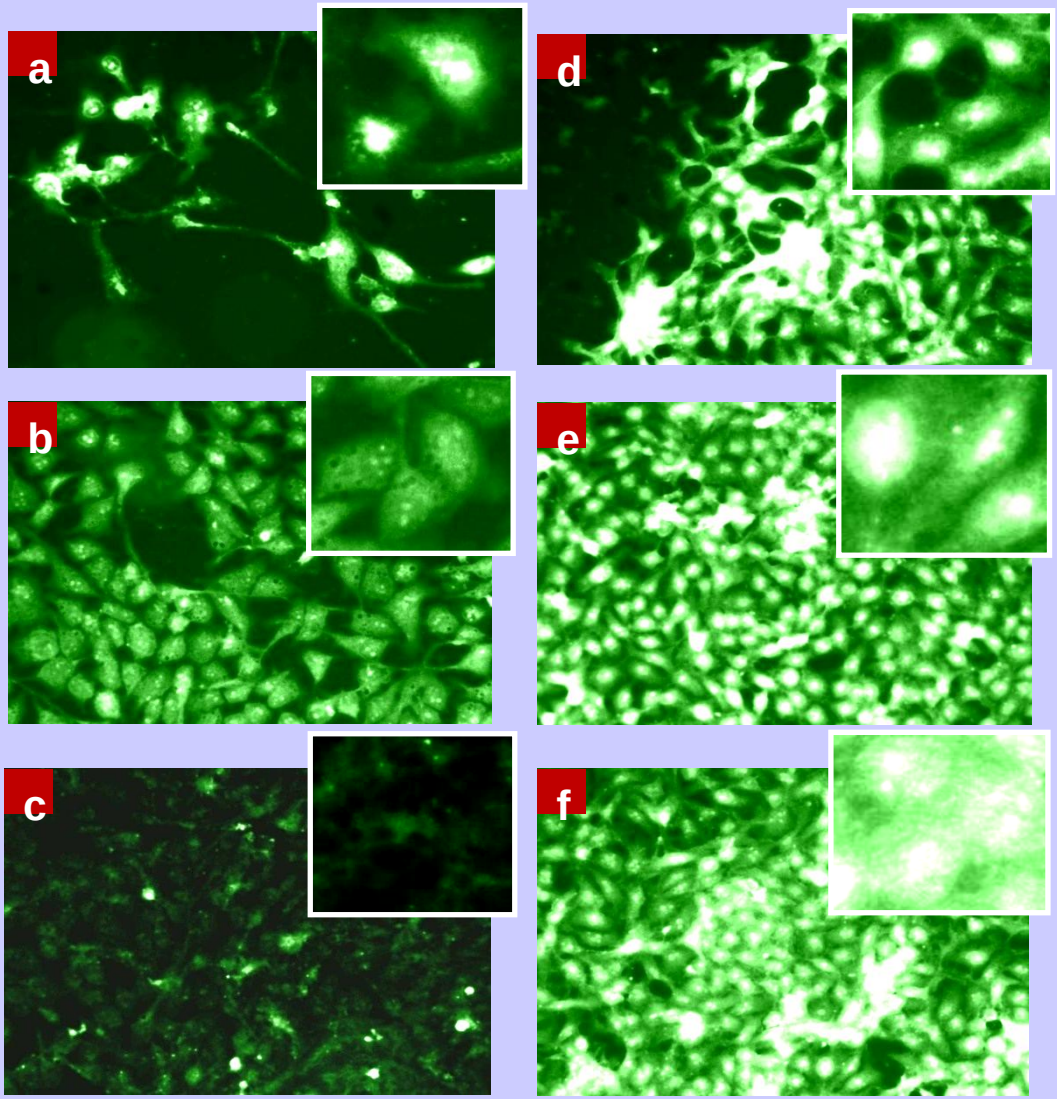

T.Serdiuk,V.Lysenko, B.Mognetti, V.Skryshevsky, A.Geloen, J. Biophotonics 6, 291 (2013)

OUTLOOK: Killing of cancer cells by SiC QDs

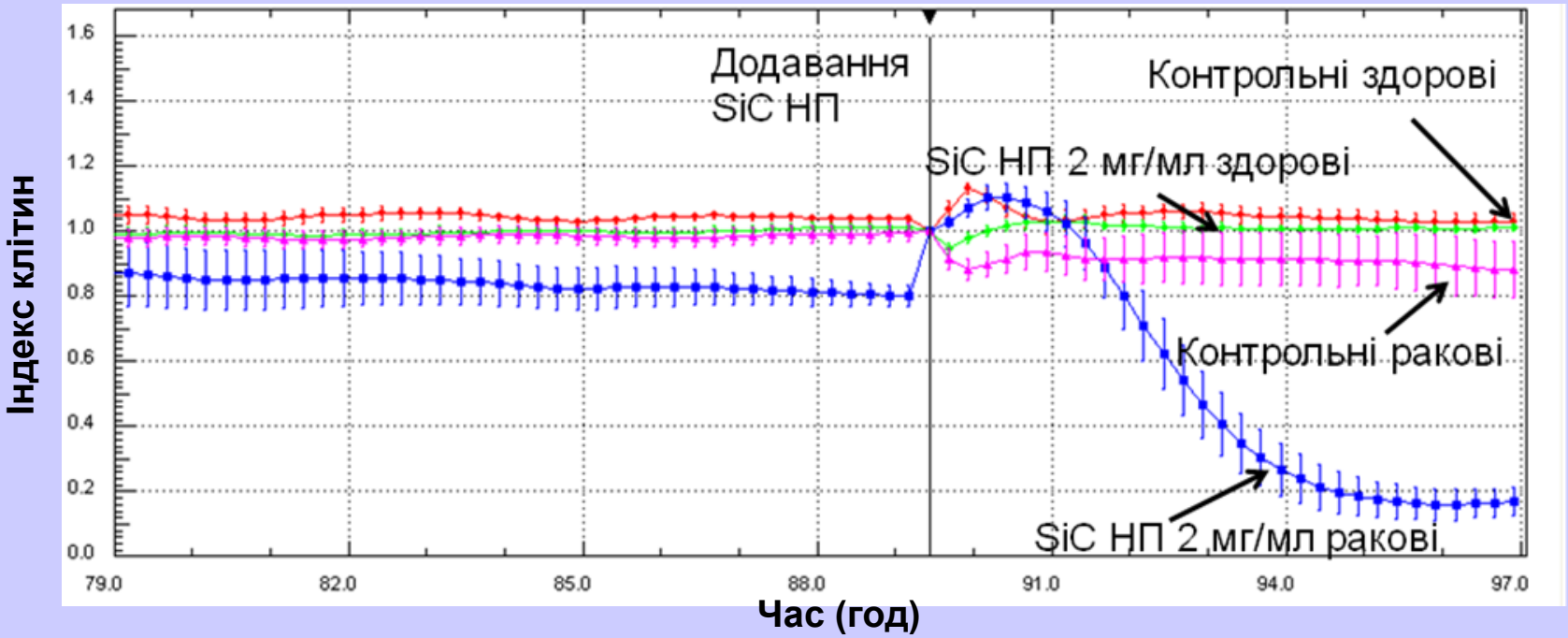

Виживанние здорових (SG) и ракових (HSC-2) клеток при инкубации QDs SiC.

OUTLOOK: QDs photodynamic therapy

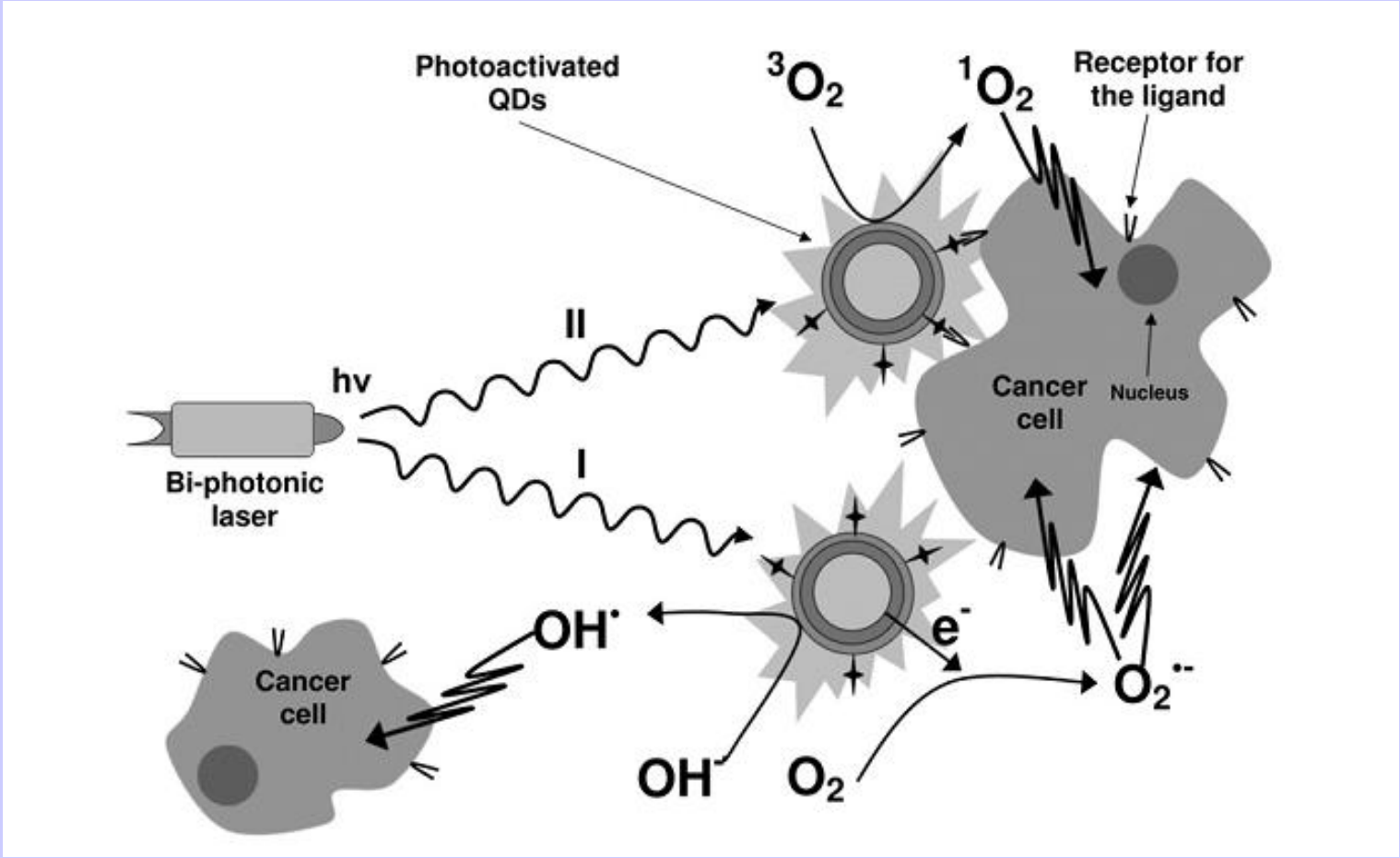

Two pathways of QD-based free radical generation applied in photodynamic therapy. Path I involves electron transfer, and path II proceeds with singlet oxygen generation.

M.Geszke-Moritz, et al, Mater.Sci.Eng.C 33 (2013) 1008

Electroless metal introduction into the Si pores

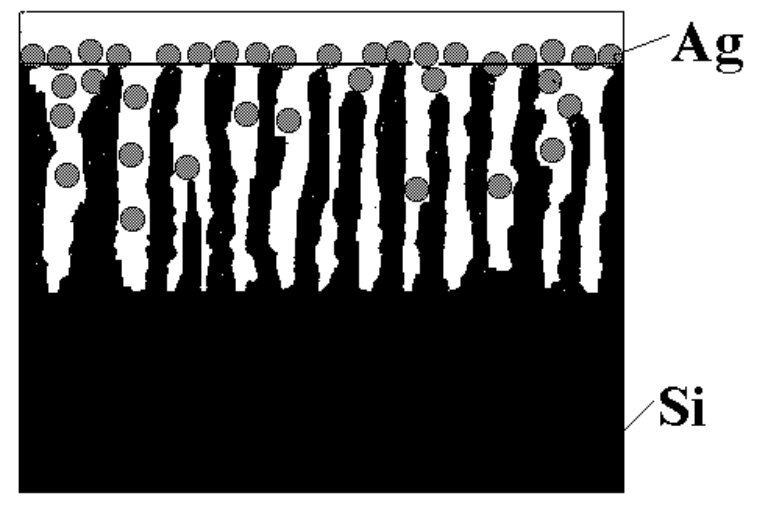

$$Ag^{+} + e_{vb}^{-} \rightarrow Ag^{0}(s)$$

$$Si(s) + 2H_2O \rightarrow SiO_2 + 4H^{+} + 4e_{vb}^{-}$$

$$SiO_2(s) + 6HF \rightarrow H_2SiF_6 + 2H_2O$$

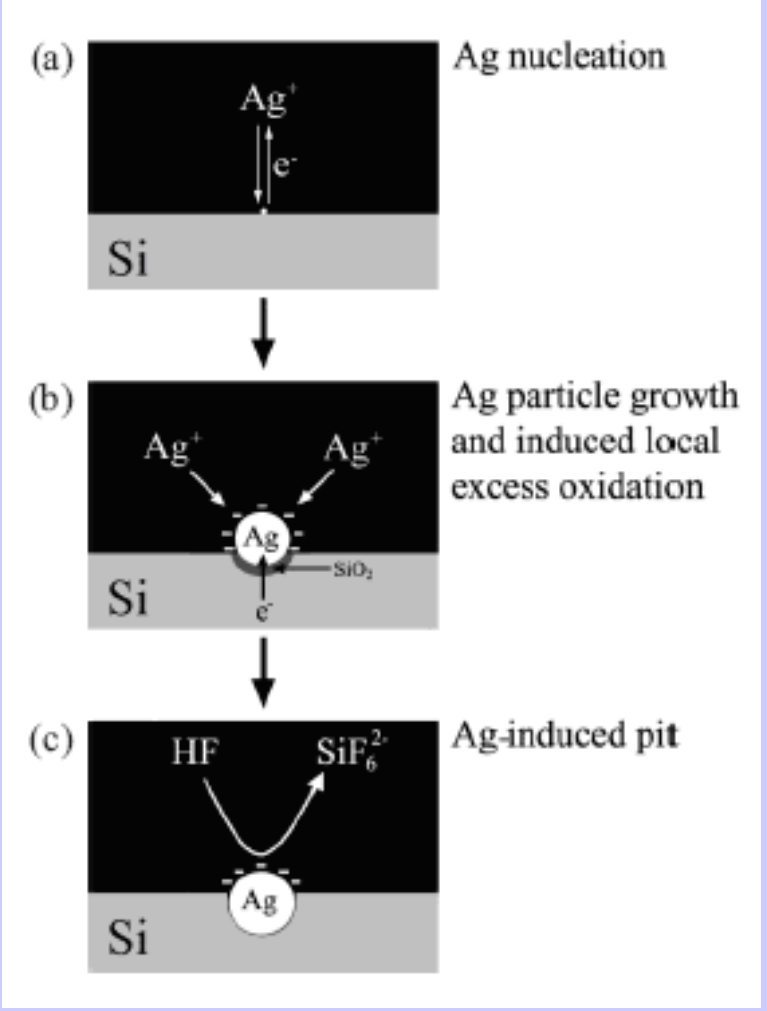

Mechanism of electroless Ag deposition on Si in HF/AgNO3 solution.

Electroless deposition of metal on Si: the working principle is the galvanic displacement reaction. The reduction of metal ions (cathodic process and oxidation of Si atoms (anodic process) occur simultaneously at Si surface, while the charge is exchanged through the Si substrate

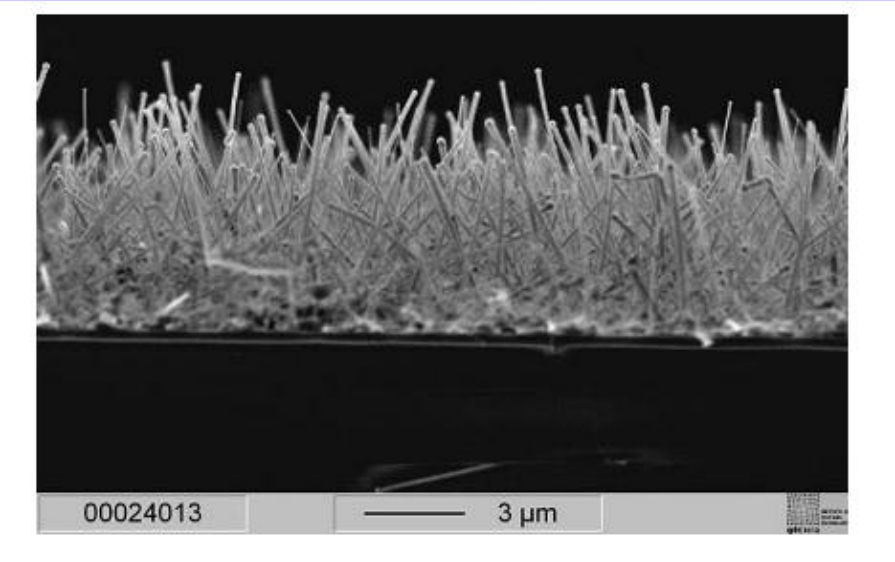

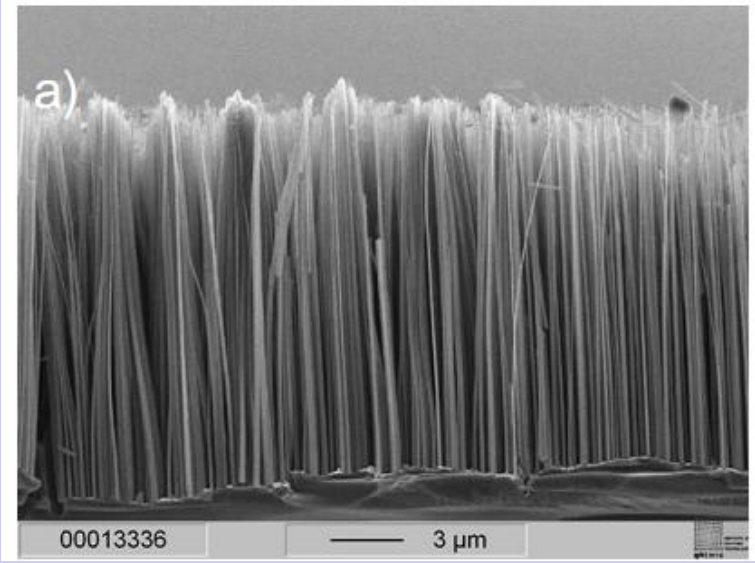

. SEM image of a Si NW carpet grown from Au nanoparicles (150 nm diameter) on a multicrystalline Si wafer (a) and etched into Si wafer

Surface Enhanced Raman Scattering of Small Molecules from Ag coated Si pores

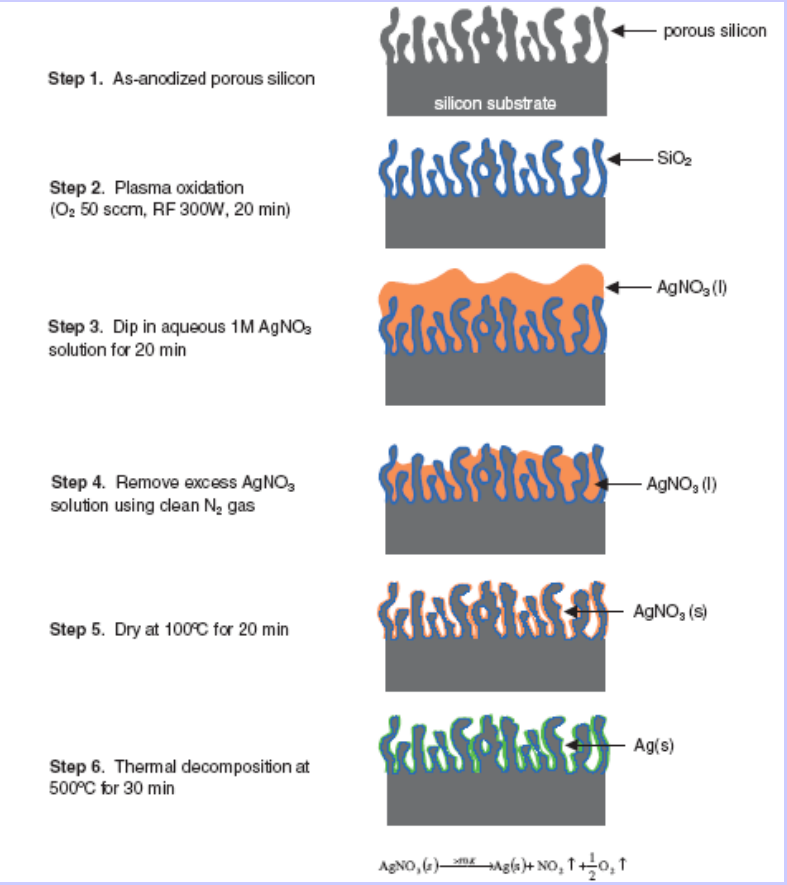

S.Chan, Adv.Mat, 2003, 15, 1595

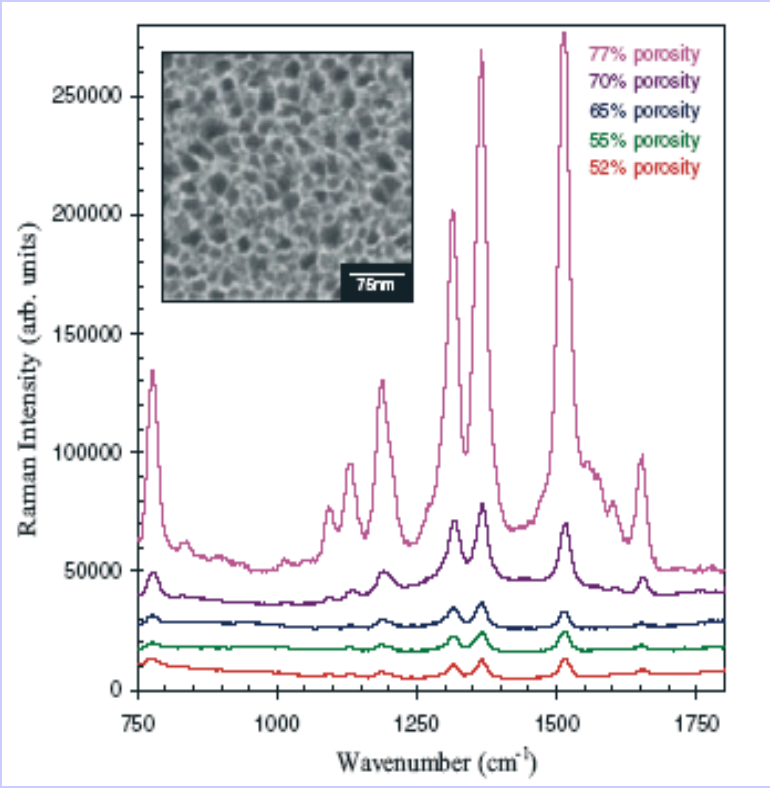

SERS of rodamine 6G

Raman spectroscopy may be used to detect nucleotides, purines or pyrimidines

V.Tolstoy, I.Chernysheva, V.Skryshevsky, Handbook of IR spectroscopy of superthin films, Wiley, N.Y., 2003

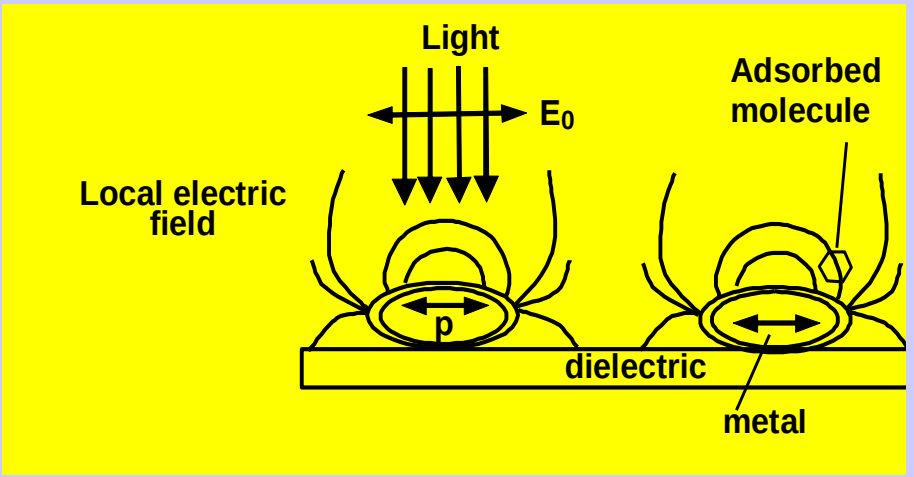

Straining of c-Si thin film with PS substrate

c-Si wafer, 150 μm

anodization

c-Si thin film, ~50 nm

PS nanostructure, 150 μm

Low T oxidation

Strained c-Si thin film, ~50 nm

Strained PS nanostructure, 150 μm

Straining of thin Si films with use of bulk partially oxidized PS nanostructure

Raman spectra (LO phonon) of PS and thin c-Si films

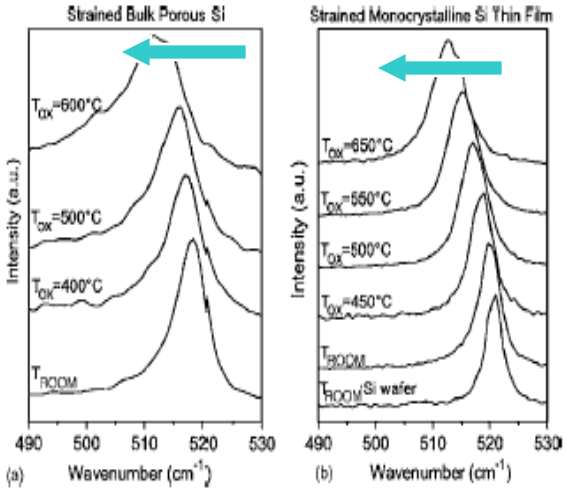

Biaxial X-Y in plane stress

$$\sigma(MPA) = -250 * \Delta\omega(cm^{-1})$$

Lattice strain

$$\xi(\%) = 0.15 * \Delta\omega(cm^{-1})$$

Up to 1.4%

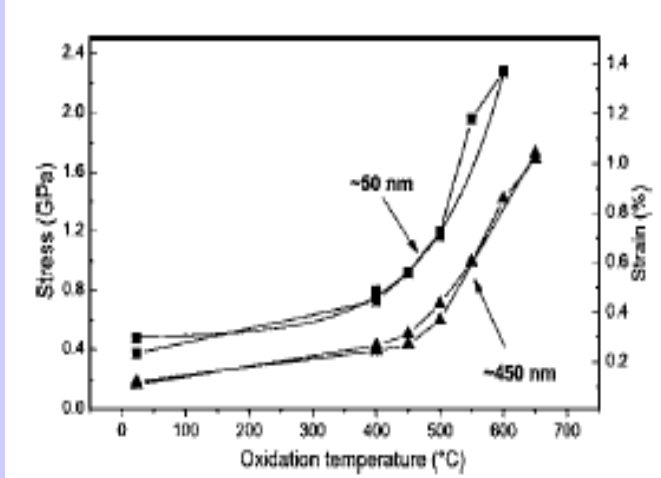

O.Marty, T.Nychyporuk, V.Lysenko, Appl.Phys.Lett, 88, 101909, 2006

Графен

н (*graphene*) — двумерная модификация углерода образованная слоем атомов С толщиной в один атом, находящихся в sp^3 гибридизаци и соединённых посредством σ- и π-связей в гексагональную двумерную кристаллическую решетку. Его можно представить как одну плоскость графита, отделённую от объёмного кристалла. По оценкам, графен обладает большой механической жесткостью и рекордно большой теплопроводностью (~1 ТПа и ~$5 \cdot 10^3$ Вт·$м^{-1}$·$К^{-1}$ соответственно). Высокая подвижность носителей заряда (максимальная подвижность электронов среди всех известных материалов) делает его перспективным материалом для использования в самых различных приложениях, в частности, как будущую основу наноэлектроники и возможную замену Si в СБИС. Основной из существующих в настоящее время способов получения графена в условиях научных лабораторий основан на механическом отщеплении или отшелушивании слоёв графита от высокоориентированного пиролитического графита (HOPG). Он позволяет получать наиболее качественные образцы с высокой подвижностью носителей. Этот метод не предполагает использования масштабного производства, поскольку это ручная процедура. Другой известный способ — метод термического разложения подложки SiC— гораздо ближе к промышленному производству.

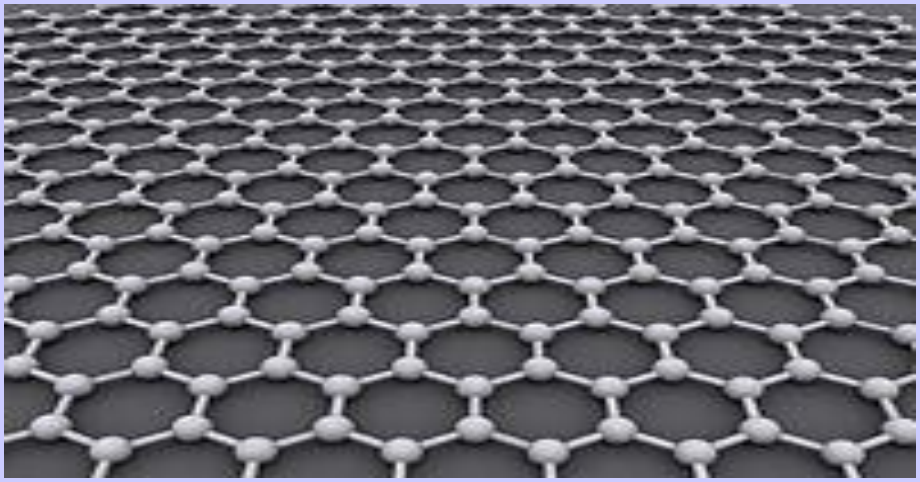

Graphene gas sensos

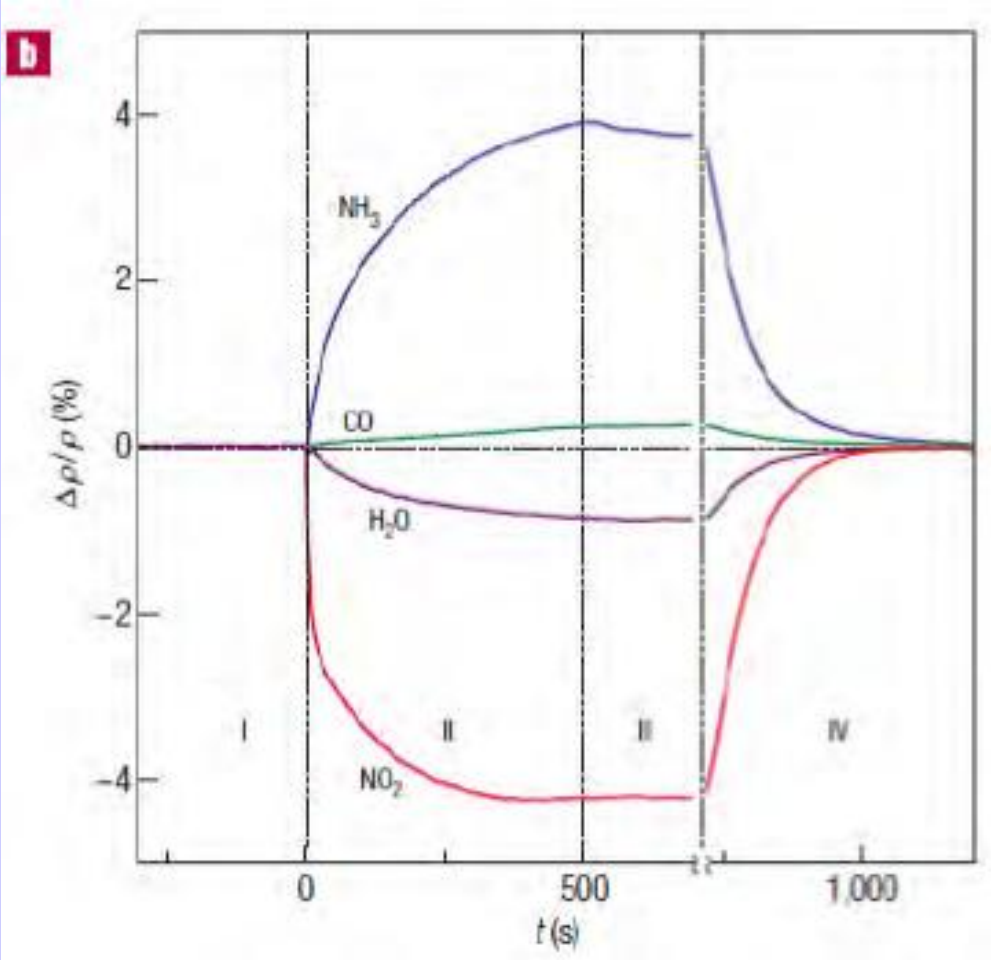

Changes in resistivity, at zero B caused by graphene's exposure to various gases diluted in concentration to 1 p.p.m.
The positive (negative) sign of changes is chosen here to indicate electron (hole) doping.
Region I: the device is in vacuum before its exposure;
II: exposure to a 5 l volume of a diluted chemical;
III: evacuation of the experimental set-up; and
IV: annealing at 150 C.

Four-point resistance sensors

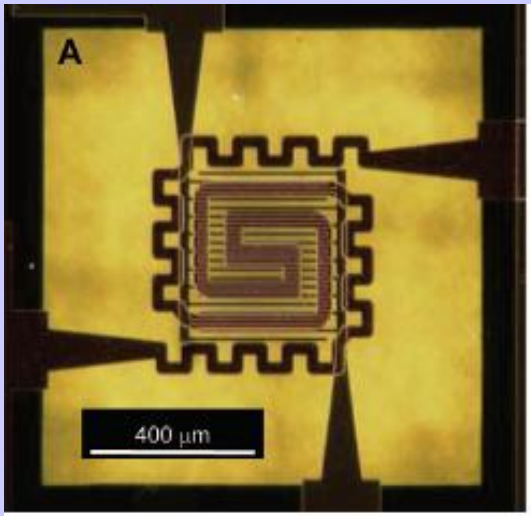

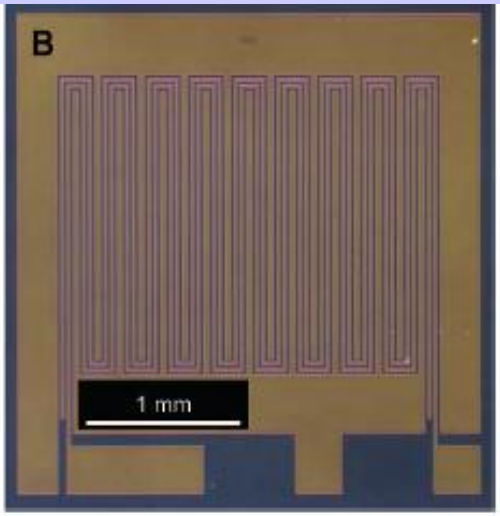

Figure 1. Photographs of the sensor substrates used. (A) Micro hot plate (MHP) sensor showing interdigitated electrodes layered over heater leads. The electrode array is a 400 μm square with individual electrodes 10 μm wide with 10 μm gaps. The sensor is suspended on a thin silicon nitride membrane. (B) Four-point interdigitated electrode sensor. Two serpentine electrodes between the interdigitated electrodes are used for four-point resistance measurements. The electrode array is 2.4 mm × 1.9 mm with 20 μm

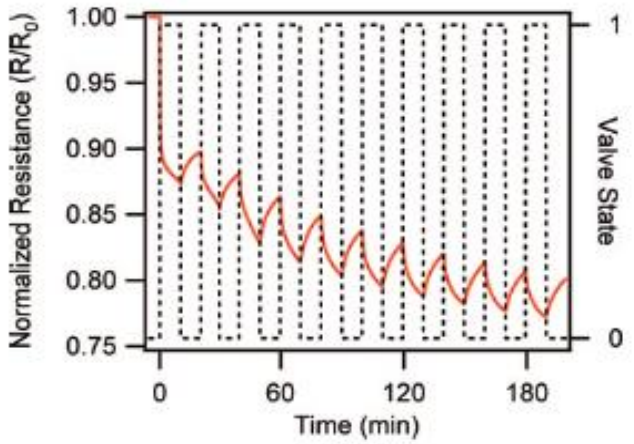

Figure 4. NO_2 detection using a graphene film. The sensor has gold electrodes and measurement used a four wire method with 500 μA driving current. The NO_2 concentration is 5 ppm in dry nitrogen.

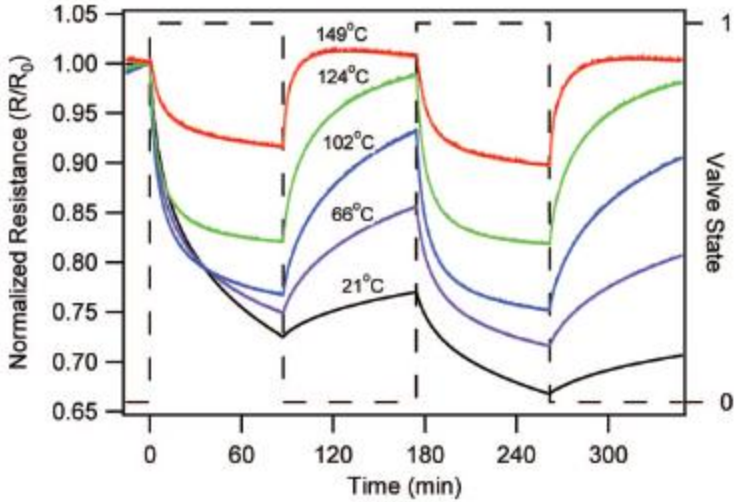

Figure 8. NO_2 detection (5 ppm) on the micro hot plate (MHP) sensor at temperatures ranging from 21 to 149 °C as indicated.

Fowler et al. ACS Nano (2009) Vol 3(2)

Highly sensitive and selective detection of NO_2 using epitaxial graphene on 6H-SiC

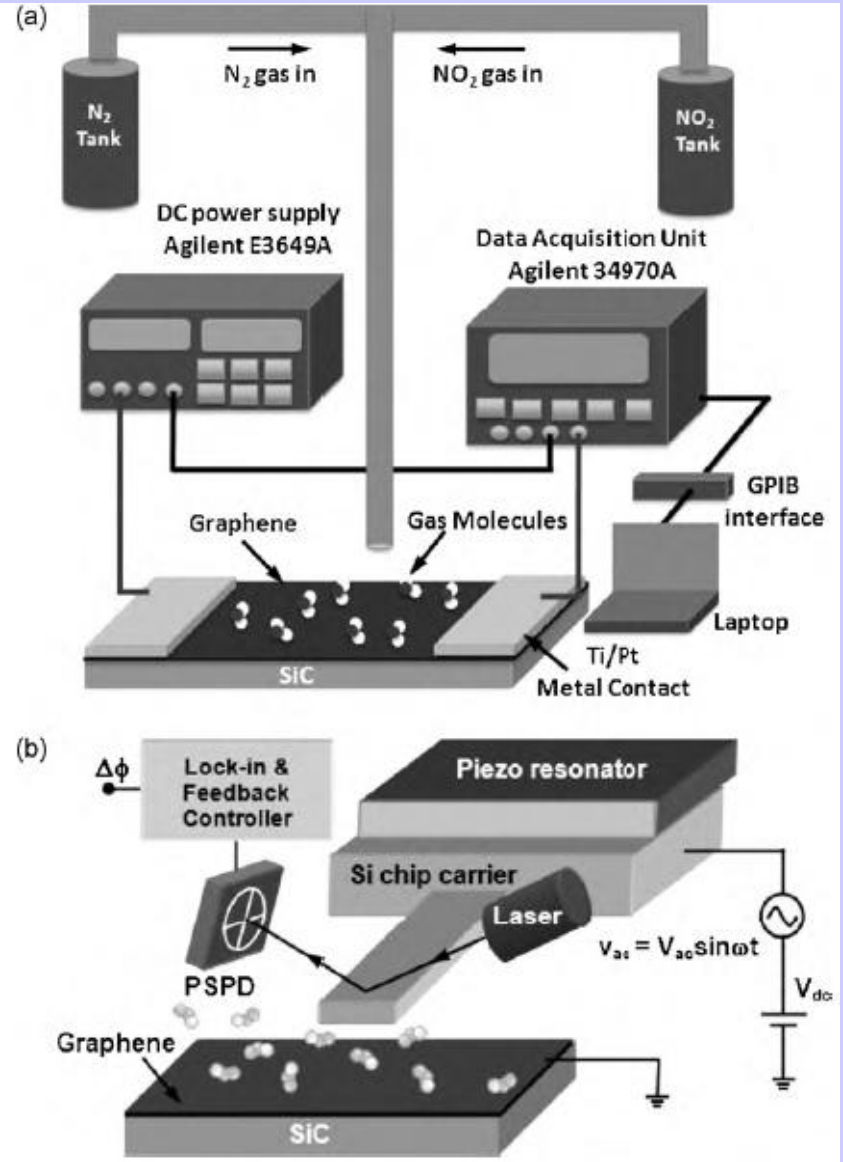

Fig. 2. (a) Amperometric and (b) potentiometric measurement setup for NO_2 sensing.

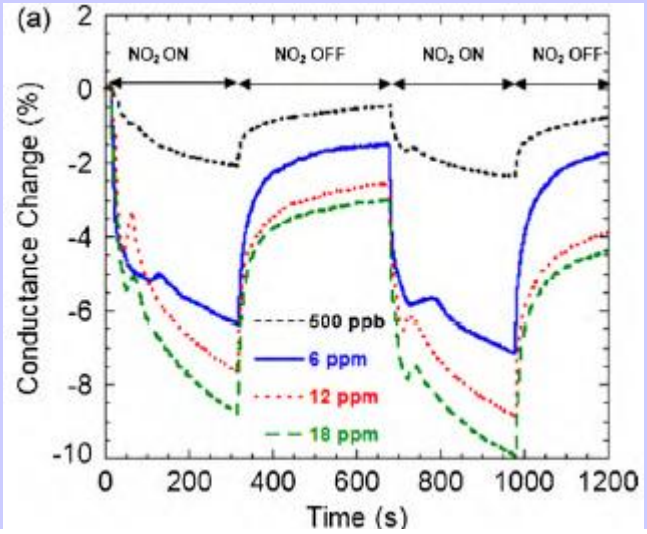

Fig. 3. The percentage conductance changes of epitaxial graphene layers grown on (a) the Si-face, and (b) the C-face of SiC for the flow of different NO_2 concentrations.

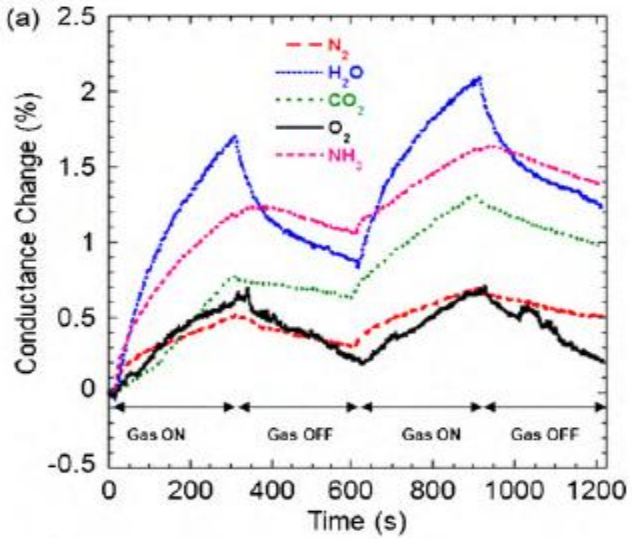

Fig. 5. The change in graphene conductance for (a) the Si-face, and (b) the C-face with the flow of major interfering gases such as N_2 (pure) NH_3 (550 ppm), CO_2 (20%), O_2 (pure), and H_2O (saturated).

Nomani et al. Sens. Actuator B (2010) Vol 1

Organic vapor sensor

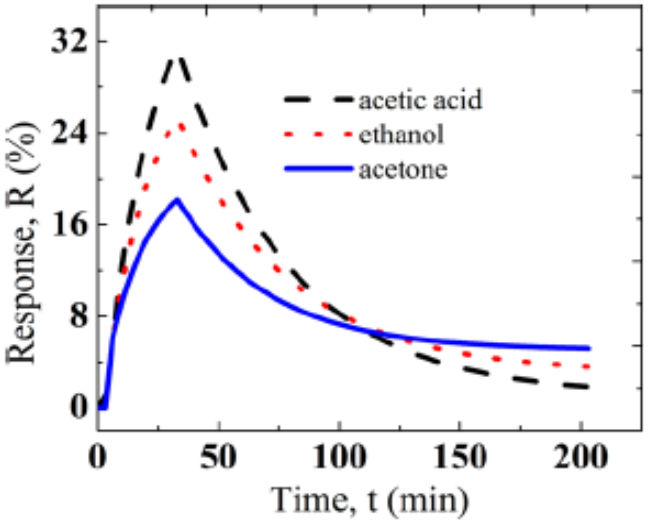

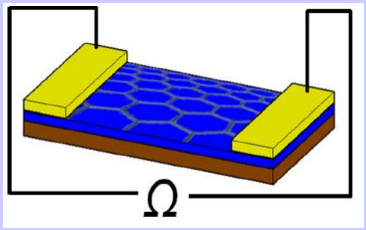

$$C_2H_5OH(ads) + 6O^-(ads) \rightarrow 2CO_2 + 3H_2O + 6e^-. \quad (3)$$

$$(CH_3)CO(ads) + 8O^-(ads) \rightarrow 3CO_2(g) + 3H_2O(g) + 8e^-.$$

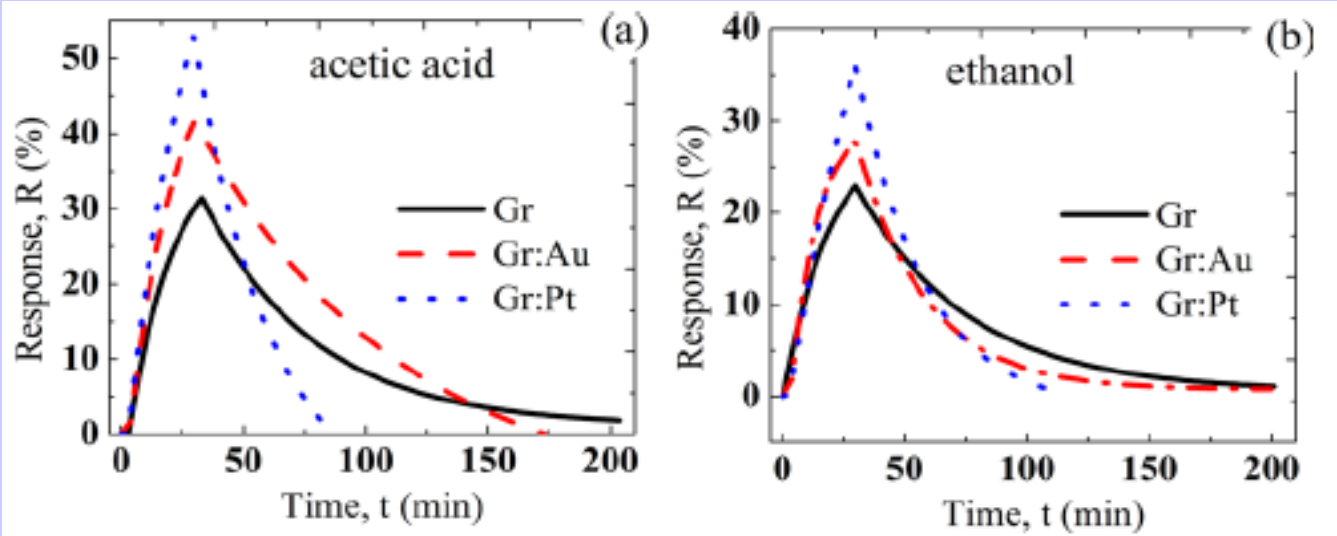

FIG. 5. A comparison of dynamic responses with three different surfaces (bare graphene (Gr), graphene decorated with gold (Gr:Au) and platinum (Gr:Pt) nanoparticles) for (a) acetic acid vapors and (b) ethanol vapors.

Gautam et al. J Appl.Phy (2012) Vol 112

Graphene glucose sensor

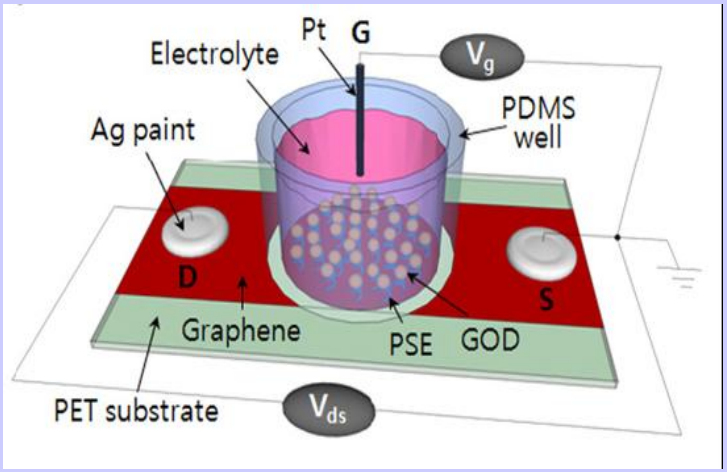

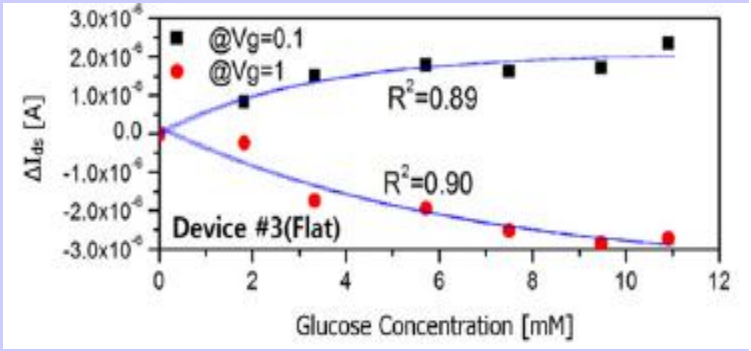

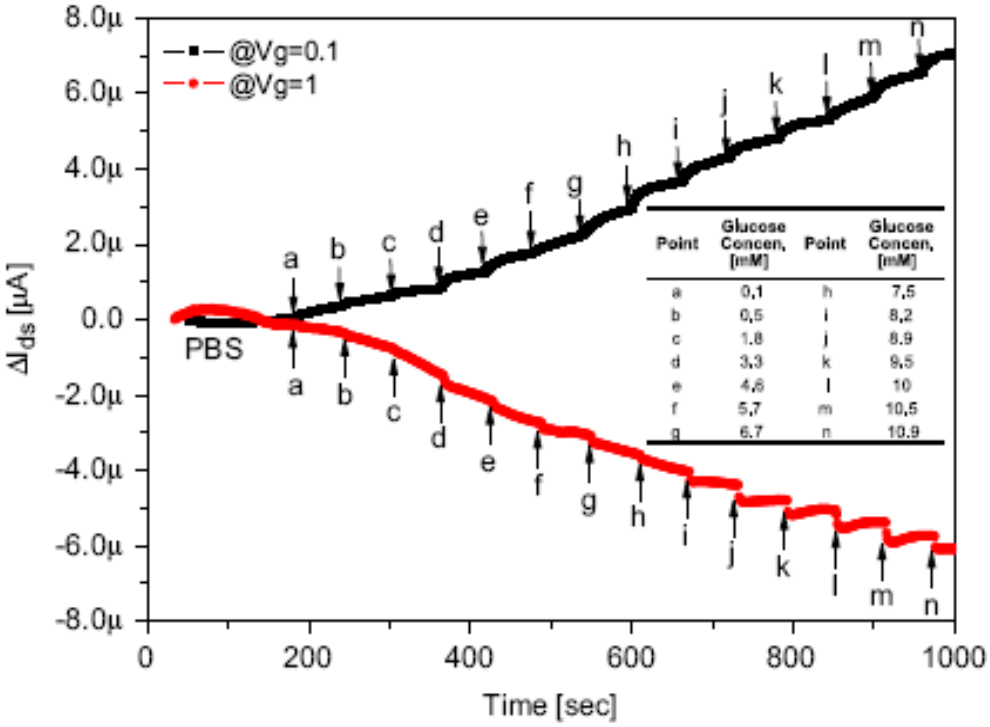

Point	Glucose Concen. [mM]	Point	Glucose Concen. [mM]
a	0.1	h	7.5
b	0.5	i	8.2
c	1.8	j	8.9
d	3.3	k	9.5
e	4.6	l	10
f	5.7	m	10.5
g	6.7	n	10.9

Fig. 5. The glucose response for the sequential concentration increase. Changes of drain-source current with $V_g = 0.1$ V and $V_g = 1.0$ V for the fixed drain-source voltage of $V_d = -0.2$ V. Starting with a pure PBS solution, the glucose was first injected at 180 s and added every minute thereafter. The glucose response for the sequential concentration increase showed a fairly enough resolution as well as continuity, which transcripts the efficacy as a clinically acceptable flexible glucose sensor.

Y.H. Kwak et al.,Biosensors and Bioelectronics 37 (2012) 82–87

Table 1 Typical gas sensors based on graphene materials (G = graphene)

Graphene material	Type of sensors	Target gas	Sensitivity	LOD	Response time	Ref.
Mechanically exfoliated G	Hall geometry	NO_2	$\Delta R > 2.5\ \Omega$ for one electron	1 molecule	6 s	73
Mechanically exfoliated G	Chemiresistor	CO_2	0.17% ppm^{-1} $(\Delta G/G_a)$	—	8 s	78
CVD grown G	Chemiresistor	N_2O	3.11×10^{-6} ppt^{-1} $(\Delta G/G_0)$	103 ppt	Few min	90
		O_2	8.87×10^{-6} ppt^{-1} $(\Delta G/G_0)$	38.8 ppt	Few min	
		SO_2	5.88×10^{-6} ppt^{-1} $(\Delta G/G_0)$	67.4 ppt	Few min	
		NO	2.51×10^{-3} ppm^{-1} $(\Delta G/G_0)$	158 ppq	5 min	
Epitaxial grown G	Chemiresistor	NO_2	0.025–0.1 $(\Delta G/G_0)$	—	5 min	95
RGO	Chemiresistor	DMMP	0.122 ppm^{-1} $(\Delta R/R_0)$	—	18 min	107
RGO	SAW	H_2	1.7 kHz for 1% H_2	—	~1 min	69
		CO	7 kHz for 1000 ppm CO	—	~1 min	
Chemically modified G	Chemiresistor	NO_2	0.443 ppm^{-1} $(\Delta G/G_0)$	3.6 ppm	5 min	71
Porous G	FET	NO_2	0.0432 ppm^{-1}	15 ppb	5–7 min	111
		NH_3	0.0071 ppm^{-1} $(\Delta R/R_0)$	160 ppb		
G/PPr	Chemiresistor	Toluene	9.84×10^{-4} ppm^{-1} $(\Delta G/G_0)$	—	Tens of s	109
G/ZnO	Chemiresistor	Ethanol	2.1 ppm^{-1} (R_a/R_g)	—	—	119
G/SnO_2	Chemiresistor	H_2S	2.1 ppm^{-1} (R_a/R_g)		5 s	116
G/Pd	Chemiresistor	NO	0.04 (2 ppb) $(\Delta G/G_0)$	—	4 min	50

Table 2 – Comparison of gas sensing characteristics of different nano-structured materials.

Material	Zinc oxide			Reduced graphene oxide				Pt-Graphene	ZnO–GrO nanocomposite		
Working temperature	350 °C			Room temperature				Room temperature	Room temperature		
Sensor characteristics											
Sensing gas	NO_2	CO	NH_3	NH_3		NO_2		H_2	CO	NH_3	NO
Analyte conc.	1 ppm in air	50 ppm in air	–	5 ppm in dry N_2	1% NH_3 in air	5 ppm in dry N_2	2 ppm in air	4% vol in air	22 ppm in dry N_2	1 ppm in dry N_2	5 ppm in dry N_2
Sensor response	~+80% ΔR[a]	Not sensitive[d]	–	~+10% ΔR	~+11.1% ΔG [b]	~−30% ΔR	~+12% ΔG	~+16% ΔR	~+24.3% ΔG	~+24% ΔG	~−3.5% ΔG
Response time (min)	~3–6		–	>10	40	>10	40	~9	~5[c]	~6[c]	~25
Recovery time (min)	>5		–	10	~30	10	~30		~2–5	~2–3	
Reference	[44]	[41]		[20]	[43]	[20]	[43]	[42]	Current work		

[a] Gas sensitivity is expressed as % change in resistance of gas sensor.

[b] Gas sensitivity is expressed as % change in conductance of gas sensor.

[c] Excludes time required for establishment of percolation network.

[d] Undoped ZnO normally is not very sensitive to CO so typically ZnO doped with SnO_2, Ni, Cu, etc. is used.